Assessment of smoke plume height products derived from multisource satellite observations using lidar-derived height metrics for wildfires in the western US

Jingting Huang[1,*], S. Marcela Loría-Salazar[2], Min Deng[3], Jaehwa Lee[4,5], Heather A. Holmes[1]

[1] Department of Chemical Engineering, University of Utah, Salt Lake City, 84112 UT, USA
[2] School of Meteorology, University of Oklahoma, Norman, 73072 OK, USA
[3] Environmental and Climate Sciences Department, Brookhaven National Laboratory, Upton, 11973 NY, USA
[~~4~~5] Earth System Science Interdisciplinary Center, University of Maryland, College Park, 20740 MD, USA
[~~5~~4] NASA Goddard Space Flight Center, Greenbelt, 20771 MD, USA

Correspondence to: Jingting Huang (jingting.huang@utah.edu)

Abstract. As wildfires intensify and fire seasons lengthen across the western U.S., the development of ~~applicable~~ models that can predict ~~the density of~~ smoke plume~~s~~ concentrations and track wildfire-induced air pollution exposures has become critical. Wildfire smoke plume height is a key indicator of the vertical placement of plume mass emitted from wildfire-related aerosol sources in climate and air quality models. With advancements in Earth observation (EO) satellites, spaceborne products for aerosol layer height or plume injection height have recently emerged with increased global-scale spatiotemporal resolution. However, to evaluate column radiative effects and refine satellite algorithms, vertical profiles of regionally representative aerosol ~~data~~properties from wildfire ~~emission~~s need to be measured directly ~~in the field~~. In this study, we conduct~~ed~~ the first comprehensive evaluation of four passive satellite remote sensing techniques specifically designed to retrieve plume height ~~distribution for wildfire smoke~~. We compared these satellite products with the airborne Wyoming Cloud Lidar (WCL) measurements during the 2018 Biomass Burning Flux Measurements of Trace Gases and Aerosols (BB-FLUX) field campaign in the western U.S. Two definitions, namely "plume top" and "extinction-weighted mean plume height", ~~are~~were used to derive representative heights of wildfire smoke plumes, based on the WCL-derived~~retrieved~~ vertical aerosol extinction coefficient profiles. Using these two definitions, w~~W~~e ~~also~~ performed a comparative analysis of multisource satellite-derived plume height products for wildfire smoke ~~using these two definitions~~. W~~ith~~e ~~the aim to~~ provided a discuss~~ion on~~ which satellite product is most appropriate~~,~~ for ~~under various aerosol loadings and in~~ determining plume height characteristics near a fire-event location or estimating downwind plume rise equivalent height, under various aerosol loadings. Our findings highlight the importance of understanding the sensitivity of different passive remote sensing techniques on~~to~~ space-based wildfire smoke plume height observations, in order to resolve ambiguity surrounding the concept of "effective smoke plume height". As additional aerosol-observing satellites are planned~~expected to be launched~~ in the coming years, our results will inform future remote sensing missions and EO satellite algorithm development~~data selection~~. This ~~will help~~ bridges the gap between satellite observations and plume rise modeling to further investigate the vertical distribution of wildfire smoke aerosols.

1 Introduction

Characterizing the vertical extent of wildfire smoke aerosols near active fire hotspots, also known as plume injection height (PIH) or smoke aerosol layer height (ALH), is a critical task in simulating the long-range transport of wildfire smoke. From a physical perspective, the initial PIH at a fire ~~event location~~ can be described as the height where the relatively stable vertical atmospheric layer is located, causing the smoke plume~~s~~ to accumulate, and where the updrafts generated by the ~~plume~~ buoyancy above the fire

source to terminate ~~due to turbulence and mixing~~ (Kahn et al., 2007; Labonne et al., 2007; Paugam et al., 2015). ~~Simply put,~~ PIH is commonly viewed as the vertical height to which a buoyant plume core can lift the polluted airmass before the smoke plume~~s~~ begin to bend over horizontally (Raffuse et al., 2012). Often ~~Practically,~~ plume heights near or downwind of active fire areas are treated as ~~meant to be~~ equivalent to PIH values. W~~It has been observed that most w~~ildfire smoke plumes move horizontally in single layers through the atmosphere, but some may become stratified into ~~discrete,~~ multiple, discrete layers (Mardi et al., 2018; Deng et al., 2022b). However, it is impossible to distinguish aerosol layering at multiple heights without vertically resolved smoke aerosol profiles. Consequently, a single height value is often applied and ~~can be~~ obtained from physics-based numerical models or passive remote sensing ~~observations~~ retrievals. Regardless of whether the vertical structure of wildfire smoke aerosols is homogenous or heterogenous, a columnar plume height retrieved from satellites is considered a representative ALH. This study focuses on the smoke-specific plumes from wildfires in the western United States (WUS); therefore, we will use smoke plume height (*SPH*) ~~hereinafter~~ to denote this.

Wildfire *SPH* ~~data~~ observed from space has ~~witnessed a significant~~ advance~~dment~~ in spatiotemporal resolution since the 2000s (Kahn et al., 2007; Ichoku et al., 2012; Lyapustin et al., 2019; Kahn, 2020). Passive satellite sensors are ~~most widely~~ used to map global wildfire *SPH* distribution, spanning a ~~substantial~~ range of recently developed techniques and retrieval algorithms. It is important to note that each method to obtain satellite *SPH* retrievals utilizes a distinct remote sensing technique, resulting in inconsistent definitions of *SPH*. To shed light on their differences, a brief overview of these methods is provided to demonstrate why they yield differing plume height interpretations.

The photogrammetric stereo capability of the Multi-Angle Imaging SpectroRadiometer (MISR) aboard the National Aeronautics and Space Administration (NASA) Earth Observing System's Terra spacecraft (Diner et al., 1998), combined with the MISR Interactive Explorer (MINX) tool (Nelson et al., 2008, 2013), provides ~~makes it a practical solution to determine~~ "wind-corrected" *SPH* values of elevated smoke aerosols. This approach takes into account feature displacements caused by the plume movement~~real motion of plume elements~~ and the stereo parallax shift among different camera views. Another ~~accepted mainstream~~ approach to retrieve *SPH* ~~information~~ takes advantage of the altitude dependence of absorption spectroscopic characteristics of molecular oxygen (O_2) in the A band at 759–771 nm ~~,~~ or the B band at 686–695 nm or the O_2–O_2 spectral band at 477 nm. ~~, which~~ This approach has been successfully applied to a number of passive satellite-supported instruments, including but not limited to POLDER/PARASOL (the POLarization and Directionality of the Earth's Reflectance mounted on the Polarization and Anisotropy of Reflectances for Atmospheric Sciences coupled with Observations from a Lidar platform, Dubuisson et al., 2009), MERIS/ENVISAT (the MEdium Resolution Imaging Spectrometer installed on the Environmental Satellite, Duforêt et al., 2007; Dubuisson et al., 2009), SCIAMACHY/ENVISAT (the SCanning Imaging Absorption SpectroMeter for Atmospheric CHartographY on board the Environmental Satellite, Corradini and Cervino, 2006; Sanghavi et al., 2012), GOME-2/MetOp (the Global Ozone Monitoring Experiment–2 flying on the Meteorological Operational series of satellites, Sanders et al., 2015; Nanda et al., 2018a; Michailidis et al., 2021), OMI/Aura (the Ozone Monitoring Instrument aboard the Aura spacecraft, Chimot et al., 2017, 2018), EPIC/DSCOVER (the Earth Polychromatic Imaging Camera loaded on the Deep Space Climate Observatory, Xu et al., 2019; Lu et al., 2021) and TROPOMI/S-5 P (the TROPOspheric Monitoring Instrument carried on the Copernicus Sentinel-5 Precursor mission, Griffin et al., 2020; Nanda et al., 2020; Chen et al., 2021). Other approaches utilize ~~Two more spectral channels~~ the ultraviolet (UV; 340–380 nm) or thermal infrared (TIR; 11 μm) bands, which are sensitive to the vertical distribution ~~and optical properties of highly absorbing non-spherical irregular~~ of absorbing ~~smoke~~ aerosols ~~particles, namely ultraviolet (UV) and infrared (IR) or thermal bands~~ (e.g., smoke and mineral dust) or absorptions by various gases released from fire (together with smoke aerosols), respectively. Using bands included in wide-swath passive sensors means that these approaches can provide ~~These~~

~~bands could also be used to pinpoint~~ *SPH* ~~on a~~ globally ~~scale~~. Based on the sensitivity of backward ~~near-UV or~~ UV radiance to the ~~presence of rising~~ height of absorbing aerosol ~~plume~~s (e.g., dust and smoke) in a Rayleigh scattering atmosphere (Hsu et al., 1996; Torres et al., 1998; Hsu et al., 1999), previous studies proposed an algorithm called the Aerosol Single-scattering albedo and Height Estimation (ASHE) that jointly retrieves ALH and single scattering albedo (SSA) using UV-aerosol index (UVAI), aerosol optical depth (AOD), and spaceborne lidar backscatter profile from multi-sensor measurements (Jeong and Hsu, 2008; Lee et al., 2015, 2016). In a subsequent study, Lee et al. (2020) revised the ASHE algorithm to function without the lidar backscatter profile. ~~Later, Lee et al., 2020 revised the ASHE algorithm to make it work without the requirement for the lidar backscatter profile in operational environments, of which the *SPH* product is used in this study. More recently,~~ Lyapustin et al.~~,~~ (2019) and Cheeseman et al.~~,~~ (2020) introduced the brightness temperature contrast approach that uses~~in~~ the Moderate Resolution Imaging Spectroradiometer (MODIS) ~~thermal~~ TIR band (11 ~~-~~μm) for smoke plume identification and characterization. Using this technique, daily *SPH* values are retrieved ~~records~~ on a global sinusoidal grid ~~have been issued~~ as part of the Multi-Angle Implementation of Atmospheric Corrections (MAIAC) atmospheric product MCD19A2.

~~When it comes to remotely sensed *SPH* retrievals, p~~Passive satellites excel by delivering widespread coverage on a regular basis, all while incurring minimal recurring costs and posing no risks to observers. Yet, dense smoke plumes, cloud cover, or scan gaps between adjoining orbits of sun-synchronous polar satellites can result in unsuccessful retrievals ~~fire detections~~ (Lyapustin et al., 2008). As a complement to these passive retrievals, active spaceborne lidars like CALIOP/CALIPSO (the Cloud-Aerosol Lidar with Orthogonal Polarization aboard the Cloud-Aerosol Lidar and Infrared Pathfinder Satellite Observation satellite, Winker et al., 2009) and CATS/ISS (the Cloud-Aerosol Transport System installed on the International Space Station, McGill et al., 2015) offer high-resolution vertical profiles of aerosol optical signals. While these spaceborne lidars ~~and~~ enhance the detection of thin smoke layers, ~~though~~ they are bound by a narrow, pencil-like swath ~~(Kahn et al., 2008)~~ providing limited spatial coverage, see Figure 9 in Loría-Salazar et al. (2021). Another limitation of~~Besides, these~~ remote sensing instruments on polar-orbiting satellites is that they do not resolve the diurnal variation of wildfire activity~~, unlike traditional in situ monitoring~~.

Endeavors to investigate fire behavior and their associated air quality (AQ) impacts have predominantly relied on the use of field data and satellite-based retrievals. ~~Hence, p~~Passive and active remote sensing techniques are complementary because of their different observational methods. The deliberate collocation of them provides synergistic insights into missing pieces of fire information that may not be attainable by either type of technique in isolation (Liu et al., 2019a; Sicard et al., 2019). Unfortunately, in the Intermountain West region of the U.S., there remains a lack of detailed vertical profiles of aerosol optical properties, despite recent field experiments such as Fire Influence on Regional to Global Environments and Air Quality (FIREX-AQ), Western wildfire Experiment for Cloud chemistry, Aerosol absorption and Nitrogen (WE-CAN), Biomass Burning Flux Measurements of Trace Gases and Aerosols (BB-FLUX), and Fire and Smoke Model Evaluation Experiment (FASMEE). Furthermore, to date, there is no universally accepted methodology for directly deriving ~~wildfire~~ *SPH* from aerosol extinction or backscatter vertical profiles due to the ambiguous use and definition of the term "effective *SPH*" (Xu et al., 2017). This poses a challenge particularly when one wants to compare columnar *SPH* values from passive remote sensors with ~~actively~~ retrieved three-dimensional (3D) distribution of smoke aerosol vertical structure from active remote sensors.

The primary objective of this study is to address the central research question: ~~of~~ which *SPH* definition corresponds to the most physically relevant plume height for ~~can effectively interpret~~ a specific satellite *SPH* retrieval algorithm~~.~~? We introduce two *SPH* definitions ~~built upon~~using vertical profiles of smoke aerosol from airborne lidar data. We then quantify the sensitivity of four passive remote sensing techniques to columnar ~~wildfire~~ *SPH* observations with respect to these two definitions, accounting for the

effects of local meteorology, distance from the active fire source, and smoke aerosol loading. Meanwhile, we explore an optimal collocation strategy to compare satellite retrievals with lidar measurements, considering instrument discrepancies in observing *SPH* experimentally. To the best of our knowledge, we present the first comprehensive assessment of multiple satellite-derived ~~wildfire~~ *SPH* products compared with aircraft lidar data. It is important to note here that there were no coincident satellite-based lidar overpasses for our field campaign data; therefore, they are not included in our results. This omission underscores the difficulties in directly comparing spaceborne lidar products with data from aircraft campaigns. The results of our study clarify the meaning of "effective *SPH*" in the remote sensing and modeling communities, filling a critical gap in uniform plume height comparisons. Our findings also meet the urgent need for a suite of remotely sensed datasets to evaluate the performance of present and future dynamic smoke plume ~~dynamic~~ models and smoke modeling frameworks, or to provide inputs to these models that improve the *SPH* characterization required to model the downwind pollutant transport.

2 M~~Direct m~~easures of wildfire *SPH*

2.1 Satellite-based wildfire *SPH*

The following four space-based wildfire *SPH* retrievals ~~that are quality-controlled~~ will be discussed in our study: (1) ~~new~~ MODIS aerosol product~~s~~ using the MAIAC algorithm (MODIS/MAIAC); (2) ~~a~~ MISR-based global *SPH* database that can be accessed via the MISR Enhanced Research and Lookup Interface (MISR/MERLIN); (3) ~~new~~ VIIRS aerosol product~~s~~ using the ASHE algorithm (VIIRS/ASHE); (4) TROPOMI-based ALH product~~s~~ (TROPOMI/ALH). **Table 1** features further information about these passively remote-sensed *SPH* ~~datasets~~products.

Table 1: Summary of multisource satellite-derived plume height products.

Data Set/Version	Availability	Resolution	Instrument/Satellite	Retrieval Method	References
MAIAC-derived injection height products/collection 6.1	February 1, 2000 to present	*horizontal*: 1 km × 1km *temporal*: 16-day repeating cycle; one-to-two-day global coverage	MODIS/Terra or Aqua	Brightness temperature contrast	Lyapustin et al. (2019)
MERLIN interface for MISR plume height project /version 2	2008–2011 as well as the summers (June, July, August) of 2017 and 2018	*horizontal*: 1.1 km × 1.1 km *temporal*:16-day repeating cycle; 9-day global coverage	MISR/Terra	Multi-angle imaging	Kahn et al. (2007)
ASHE-derived ALH products/research	August of 2013–2018	*horizontal*: 6 km × 6 km *temporal*:16-day repeating cycle; daily global coverage	VIIRS/SNPP[a]	Ultraviolet radiometry	Lee et al. (2020)
TROPOMI level-2 ALH/version 1	April 30, 2018 to July 1, 2021	*horizontal*: 3.5 km × 7 km (across x along track) from April 30, 2018 to August 6, 2019; 3.5 km × 5.5 km since August 6, 2019	TROPOMI/S-5 P	Oxygen absorption	Sanders et al. (2012)

					temporal:16-day repeating cycle; near-daily global coverage		

a Data from VIIRS sensors on other satellite platforms were unavailable for this study.

Instrument	Geographic Coverage/ Satellite Orbit	Satellite/Agency	Data Set/Version	Time Period	Resolution
MODIS	global/sun-synchronous polar	Terra, Aqua/NASA	MAIAC-derived injection height products/collection 6.1	February 1, 2000 to present	*horizontal*: 1 km × 1km; *temporal*: 16-day repeating cycle; one-to-two-day global coverage
MISR	global/sun-synchronous polar	Terra/NASA	MERLIN interface for MISR plume height project /version 2	2008–2011 as well as the summers (June, July, August) of 2017 and 2018	*horizontal*: 1.1 km × 1.1 km; *temporal*:16-day repeating cycle; 9-day global coverage
VIIRS	global/sun-synchronous polar	Suomi NPP/NASA, NOAA	ASHE-derived ALH products/research	August of 2013–2018	*horizontal*: 6 km × 6 km; *temporal*:16-day repeating cycle; daily global coverage
TROPOMI	global/sun-synchronous polar	S-5 P/ESA, the Netherlands Space Office, the European Commission	TROPOMI level-2 ALH/version 1	April 30, 2018 to July 1, 2021	*horizontal*: 3.5 km × 7 km (across x along track) from April 30, 2018 to August 6, 2019; 3.5 km × 5.5 km since August 6, 2019; *temporal*:16-day repeating cycle; near-daily global coverage

2.1.1 MODIS/MAIAC

135 MODIS sensors are, located on the Terra (morning sensor, 10:30 AM local solar time) and Aqua (afternoon sensor, 1:30 PM local solar time) satellite platforms and operated in the thermal TIR spectrum, have the unique ability to detect active fires (Salomonson et al., 2002). This twin-MODIS design covers most regions on near the equator with at least four observations per day. The number of observations increases as one approaches the poles due to overlapping orbits. The MAIAC algorithm uses MODIS data to obtain near-fire-source aerosol injection heightAtmospheric properties data created on the MODIS aerosol data using the MAIAC

140 algorithm, known as the MCD19A2 dataset with high resolution (1 km), offers information on near-fire-source aerosol injection height.

By assuming a fixed lapse rate, the MAIAC PIH algorithm utilizes negative thermal contrast at 11 μm between smoke and sufficient neighboring smoke-free pixels and converts the colder brightness temperature into *SPH* estimateions (Lyapustin et al., 2019; Cheeseman et al., 2020). The valid range allowed for the MAIAC-based *SPH* is up to 10 km. However, the *SPH* calculation

145 struggles with large smoke areas and small fires emitting low levels of absorbing gases, meaning it requires a high enough plume opacity (AOD at 470 nm $\geq$ 0.8) to obtain a useful signal. WAdditionally, when compared to other *SPH* datasets such as MISR and CALIOP, the MAIAC method tends to significantly underestimate the height of smoke plumes, particularly for transporting dilute smoke downwind of the fire (Lyapustin et al., 2019)over time and distance from the source of burning. In spite of these limitations,

the MAIAC algorithm provides valuable ~~data~~ information within approximately 75–150 km of the identified thermal hotspots, i.e., fire ~~for optimal retrieval quality~~ (Loría-Salazar et al., 2021).

2.1.2 MISR/MERLIN

With its nine fixed push-broom cameras, MISR aboard NASA's Terra satellite captures images ~~with high precision~~ from nine different angles and four spectral bands, allowing for studies of wildfire and aerosol distributions using stereoscopic techniques, unaffected by bright surfaces (Moroney et al., 2002; Muller et al., 2002). The wealth of data collected by the MISR instrument over two decades offers valuable insights into the global climatology of fire in the environment, ~~categorized by various~~ across geographic regions, biomes, and seasons (Val Martin et al., 2018; Gonzalez-Alonso et al., 2019). ~~This~~ The publicly available database built using manually postprocessed MISR products has been used to ~~validate~~ evaluate plume rise ~~in~~ models (e.g., Ke et al., 2021) and other satellite-derived datasets (e.g., Lyapustin et al., 2019; Griffin et al., 2020). Recently, an ~~novel~~ interactive visualization tool called MERLIN ~~has been~~ was developed to ~~cover applications of the outdated MISR Plume Height Project and~~ facilitate the exploration and accessibility of over 70,000 records of global wildfire plume ~~data~~ height retrievals (Boone et al., 2018; Nastan et al., 2022).

MISR's global *SPH* mapping, with a 250–500 m vertical resolution, complements aerosol height curtains obtained from spaceborne lidar systems (Kahn et al., 2007, 2008; Val Martin et al., 2018). However, Tosca et al. (2011) found that stereo-derived *SPH* from MISR was significantly lower than the top altitude observed by CALIOP for the 2006 Indonesian fires. Nevertheless, important lessons can be drawn from the underestimated *SPH* values in the MISR product as follows: (1) the overpass time of MISR in the morning precedes the daytime peak in fire activity, typically in late afternoons when temperatures are highest and relative humidity is lowest; (2) very few coincident overpasses exist over fires during a short time of interest due to the narrow MISR swath, which allows global coverage only approximately once per week. Additionally, the revisit period of MISR for a specific geographical spot varies from 2 to 9 days, depending on the latitude (Kahn et al., 2007); (3) MISR automated stereoscopic image's dependence on optically distinct plume-like features for accurate height estimation can introduce bias, mainly when dealing with thin smoke or smoke downwind of the active fire source with less defined boundaries (Nelson et al., 2013). However, ~~The~~ blue-band data at 1.1 km horizontal cell size is considered a better choice for capturing the higher injection heights associated with fine smoke aerosols than the corresponding red-band retrievals at the spatial resolution of 275 m (Nelson et al., 2013). In this study, we extracted blue-band, wind-corrected heights with "good" quality flags downloaded from MERLIN. This preference is due to the blue band's (446.4 ± 41.9 nm) sensitivity to thinner aerosol layers, enabling the detection of aerosol features at higher altitudes.

2.1.3 VIIRS/ASHE

The launch of ~~subsequent~~ operational VIIRS sensors has been planned for the Joint Polar Satellite System (JPSS) series since 2011, in anticipation of the post-MODIS era (Cao et al., 2013a, 2013b; Goldberg et al., 2013; Wolfe et al., 2013; Wang and Cao, 2019). VIIRS currently flies on three polar-orbiting satellites: Suomi National Polar-orbiting Partnership (SNPP), National Oceanic and Atmospheric Administration-20 (NOAA-20) and NOAA-21 satellites. This study uses data from SNPP VIIRS. The VIIRS instrument has a wide swath of 3,040 km and can observe the entire Earth twice a day — once during the day and once during the night. There are some overlaps between consecutive swarths, which means that ~~Owing to a large image swath of 3,040 km and a 12 h global coverage revisiting cycle,~~ mid-latitudes will experience up to 4 looks per day (Wolfe et al. 2013). Even though the SNPP VIIRS data has enhanced radiometric measurement quality, a broad spectral range, and a fine spatial resolution (Csiszar et al., 2014; Schroeder et al., 2014), the limited temporal information ~~12 h overpass time lag~~ may curtail its efficacy for delineating

fire perimeters and assessing fire spread, especially during short fire durations (Cardil et al., 2019).

The research version of the ASHE algorithm (transition to operational processing is underway at the time of writing) provides the plume height of UV-absorbing aerosols like smoke and dust over broad areas, including both near-source and transported plumes (Loría-Salazar et al., 2021). Initially, it leveraged AOD and Ångström Extinction Exponent (AEE) from the MODIS or VIIRS aerosol product in its retrieval process, as well as ALH along the CALIOP track as a constraint (Jeong and Hsu, 2008; Lee et al., 2015). By assuming spatially invariant SSA retrieved along the CALIOP track over a MODIS/VIIRS granule, ~~it has shown~~ the ~~ability to extend the~~ height retrieval can be extended beyond the narrow CALIOP track, thereby improving spatiotemporal coverage. This study makes use of a release candidate of ASHE, that ~~which can retrieve ALH bypassing the need for~~ does not use the CALIOP ~~measurements~~constraints~~,~~ ~~benefiting from the~~and leverages the synergy between VIIRS and Ozone Mapping and Profiler Suite - Nadir Mapper (OMPS-NM) for UV measurements (Lee et al., 2020). To further improve its performance, a systematic optimization of the smoke optical models used in the algorithm was carried out by iteratively comparing the retrieved ALH and SSA with those from CALIOP and ground-based measurements offline until satisfactory similarity was found between the results (e.g., Jeong et al., 2022). ~~One simplification made by the algorithm is to assume a single aerosol layer, which may not accurately reflect complex atmospheric conditions characterized by multiple aerosol layers. Also, i~~Its application is limited to UV-absorbing aerosols with moderate to thick optical depths (AOD at 550 nm > 0.5–1.0), rendering it ineffective for aerosols with lower optical depths. Preliminary evaluation suggested that the ASHE-retrieved *SPH* had an uncertainty of 1–1.2km (or 30–40% for *SPH* of 3 km) for heavy aerosol loading cases (AOD > 1) (Lee et al., 2016, 2020). The uncertainty is dependent on errors in retrieved AOD, assumed aerosol optical model, and surface reflectance, and generally decreases with increasing AOD. It should be noted that OMPS-NM abroad SNPP has a relatively coarse spatial resolution of ~50 × 50 km^2 near nadir (~200 × 100 km^2 near the edge of the across-track scan), indicating that it has limitations for small-scale (subpixel) smoke plumes. Although there are multiple VIIRS instruments, the ASHE product is currently only available for SNPP VIIRS. It is anticipated that this retrieval algorithm will be implemented for other VIIRS instruments in the future.

2.1.4 TROPOMI/ALH

The TROPOMI instrument is the single payload on board of the European Space Agency (ESA) S-5 P satellite mission, ~~running in the~~ planned ~~timeframe~~ for 2017–2024. TROPOMI is a spectrometer that monitors key atmospheric constituents and aerosol/cloud properties by observing reflected sunlight across the spectral bands in the UV, the visible (270–500 nm), the near-TIR (675–775 nm), and the shortwave TIR (2305–2385 nm). Compared to its predecessors (OMI and SCIAMACHY), TROPOMI provides high spatially resolved information and is capable of daily global coverage and near real-time data, which enables regular monitoring and rapid assessment of changes in the Earth's atmosphere (Veefkind et al., 2012).

By analyzing the spectral signature of light that is absorbed by O$_2$ in the A band in the near-TIR wavelength range between 759 and 770 nm, the TROPOMI ALH algorithm estimates the height of aerosol plumes in the atmosphere (Sanders et al., 2012; Nanda et al., 2019). It has shown to be effective in retrieving high plumes up to 8 km in height above ground level (AGL), with reduced uncertainties for thicker and lower plumes between 1 and 4.5 km in height AGL (Griffin et al., 2020), as well as for dark surfaces (Nanda et al., 2018b). However, it ~~has been~~was found to be biased low ~~in contrast to~~compared with other *SPH* datasets such as MISR and CALIOP, most likely due to its tendency to return an intermediate plume height when multiple aerosol layers are present (Griffin et al., 2020; Nanda et al., 2020). In addition, Nanda et al. (~~,~~ 2020) pointed out that cloud contamination would have an impact on the TROPOMI/ALH product since it is unable to distinguish between cloud and aerosol signals from the measured radiances. In this study, we only used data having a quality assurance value larger than 0.5 to filter mostly cloudy scenes or

retrievals~~observations~~ with geolocation errors.

2.2 Airborne lidar measurements

The 2018 BB-FLUX field campaign deployed the upward-pointing Wyoming Cloud Lidar (WCL) on the University of Wyoming King Air (UWKA) research aircraft that sampled smoke plumes from more than 20 wildfires during 35 flights over the WUS. The airborne WCL measurements of attenuated backscattering coefficient and lidar depolarization ratio were calibrated on a per-flight basis. The vertical aerosol extinction profiles (units: km^{-1}) were retrieved with Fernald's method assuming a constant lidar ratio of 60 and evaluated with in situ measurements (see Deng et al., 2022a for details). **Table 2** lists ~~the~~ nine wildfire cases ~~during August 2018 used in this paper~~, including locations, start and containment dates, and acres burned (Historic Perimeters Combined 2000–2018 GeoMAC, 2023). It also summarizes eleven flight missions from August 2018, selected for the number of collocated pairs between valid lidar transects and satellite overpasses, with the flight trajectories illustrated in ~~and~~ **Fig. 1** ~~depicts the matching eleven flight trajectories~~. The chosen flights are limited to ~~passes of~~ smoke plumes that could be attributed to a specific wildfire. Other flights during the campaign ~~are~~ were excluded from this study because they target prescribed fires, small wildfires, clouds, and ~~the air mass containing the~~ aged smoke plumes. Small fires were not included, in part, because of the expected large uncertainties in satellite retrievals of the relatively low *SPH* values (ranging from hundreds of meters for prescribed fires to thousands of meters for small fires). Large errors for smoke aerosol layers within the boundary arise from a mismatch between the coarse spatial resolution of satellite pixels and the fine-scale smoke plume variability inherent in wildfire activity (Geddes and Boesch, 2015).

We ~~then~~ re-gridded valid WCL two-dimensional (2D) transects at a vertical resolution of 3 m and an along-track horizontal resolution of about 1.1 km to calculate *SPH* and columnar AOD throughout the atmosphere. Compared to satellite observations, the re-gridded WCL measurements have a much smaller field of view in the cross-track direction, therefore the WCL can show much finer spatial variations in smoke. Moreover, it should be noted that the WCL can be fully attenuated in dense smoke and unable to detect the actual *SPH*, and the aircraft might fly above the plume bottom ~~height~~, so the upward-looking WCL only samples partial AOD of the aerosol vertical profiles, which fundamentally differs from the AOD ~~that~~ derived from satellite retrievals~~data~~.

Table 2: Summary of nine wildfire cases with its general information and the corresponding eleven flight missions ~~during~~ from August 2018 ~~that were selected based on the number of collocated pairs between valid lidar transects and satellite overpasses~~. ~~The~~ A flight name ~~because of the wildfire case occurred in the morning~~ is denoted by its date '+ a' because the flight occurred in the morning;~~,~~ otherwise, it is denoted by its date '+ b' if it occurred in the afternoon.

Wildfire Name	Active Fire Location (Latitude, Longitude)	Start Date	Approximate Containment Date	Approximate Burned Area (acres)	Flight Date (UTC)	Flight Name	Aircraft Sampling Distance from Active Fire Source (km)	Nth Day After Fire Start Date
Sharps Fire, ID	43.467°N, 114.145°W	Jul 29, 2018	Aug 12, 2018	64, 812	2018/08/03	0803a	18.88	6
					2018/08/04	0804b	46.50	7
Rabbit Foot Fire, ID	44.856°N, 114.307°W	Aug 2, 2018	Sep 19, 2018	36, 031	2018/08/08	0808b	21.86	7

Wildfire Name	Active Fire Location (Latitude, Longitude)	Fire Start Date	Fire End Date	Acres	Flight Date (UTC)	Flight Name	Aircraft Sampling Distance from Active Fire Source (km)	Nth Day After Fire Start Date
					2018/08/12	0812a	32.80	11
Watson Creek Fire, OR	42.653°N, 120.818°W	Aug 15, 2018	Sep 9, 2018	59, 067	2018/08/19	0819a, 0819b	a: 5.26/b: 22.61	5
					2018/08/24	0824a	41.75	10
					2018/08/25	0825a	13.17	11
Sheep Creek Fire, NV	40.773°N, 116.842°W	Aug 18, 2018	Aug 23, 2018	59, 789	2018/08/20	0820a, 0820b	a: 1.70/b: 1.48	3
South Sugarloaf Fire, NV	41.812°N, 116.324°W	Aug 17, 2018	Sep 3, 2018	233, 608	2018/08/23	0823a	51.44	7

Flight Date (UTC)	Flight Name	Wildfire Name	Active Fire Location (Latitude, Longitude)	Aircraft Sampling Distance from Active Fire Source (km)	Nth Day After Fire Start Date
2018/08/03	20180803a	Sharps Fire, ID	43.467°N, 114.145°W	18.88	6
2018/08/04	20180804b	Sharps Fire, ID	43.467°N, 114.145°W	46.50	7
2018/08/08	20180808b	Rabbit Foot Fire, ID	44.856°N, 114.307°W	21.86	7
2018/08/12	20180812a	Rabbit Foot Fire, ID	44.856°N, 114.307°W	32.80	11
2018/08/19	20180819a, 20180819b	Watson Creek Fire, OR	42.653°N, 120.818°W	a: 5.26/b: 22.61	5
2018/08/20	20180820a, 20180820b	Sheep Creek Fire, NV	40.773°N, 116.842°W	a: 1.70/b: 1.48	3
2018/08/23	20180823a	South Sugarloaf Fire, NV	41.812°N, 116.324°W	51.44	7
2018/08/24	20180824a	Watson Creek Fire, OR	42.653°N, 120.818°W	41.75	10
2018/08/25	20180825a	Watson Creek Fire, OR	42.653°N, 120.818°W	13.17	11
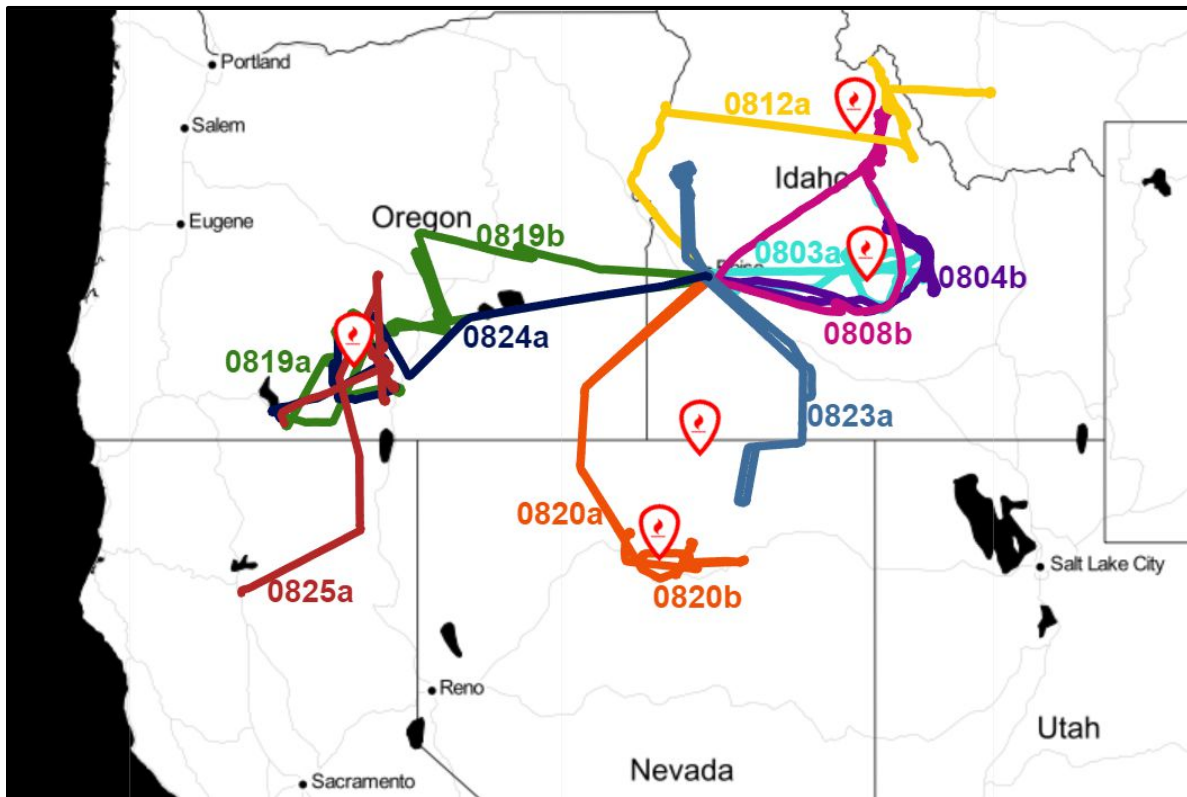
Figure 1: Color-coded eleven UWKA flight trajectories during the 2018 August BB-FLUX project, each of which ~~was~~ is associated with one of nine wildfire cases denoted by fire icons.

3 Methods

3.1 Definitions of wildfire *SPH* estimates

The extinction coefficient is a key parameter for the fundamental radiative transfer calculations of wildfire smoke aerosols from the surface to the top of the atmosphere (TOA) (e.g., Ansmann et al., 2018; Solomon et al., 2022) and can yield a linear relation to the particle mass (or volume) concentration (e.g., Mamouri and Ansmann, 2016; Toth et al., 2019; Ansmann et al., 2021). In previous studies, the aerosol extinction coefficient is ~~It has been recognized as~~ one of the most frequently observed and reported aerosol optical properties to characterize the ~~atmospheric~~ vertical structure of the atmosphere and ~~establish~~ develop a height retrieval algorithm ~~in previous studies~~ (Gordon, 1997; Dubovik et al., 2011; Sanghavi et al., 2012; Hollstein and Fischer, 2014; Ding et al., 2016; Wu et al., 2016; Xu et al., 2017). Lidar-based active remote sensing technology ~~usually delivers~~provides an attenuated backscatter signal intensity that is ~~then~~ processed by designating an extinction-to-backscatter ratio to produce vertical profile~~sing~~ of the aerosol extinction coefficient ~~by designating an extinction-to-backscatter ratio~~ (Liu et al., 2015; Rosati et al., 2016; Baars et al., 2021).

Two definitions have been proposed and widely used to derive a representative height of wildfire smoke plumes based on the vertical distribution of aerosol extinction coefficient at a given spectral wavelength from active lidar measurements. The concept of "effective *SPH*" can be defined either through smoke aerosol layer boundaries or by considering the complete vertical profile (**Fig. 2**). One method identifies the topmost height of the plumes according to the geometric boundary of the aerosol layers. Another approach ~~is deduced from~~adopts the average height of the aerosol layers, ~~-~~weighted by the extinction (or backscatter) coefficient that ~~, indicating~~reflects the radiative properties of wildfire smoke particles. In this section, we will present a detailed explanation of these two definitions and apply them to the ~~full vertical profiles of~~ WCL-measured vertical profiles of aerosol extinction

275   coefficient within the troposphere. The height hereinafter is computed in kilometers AGL.
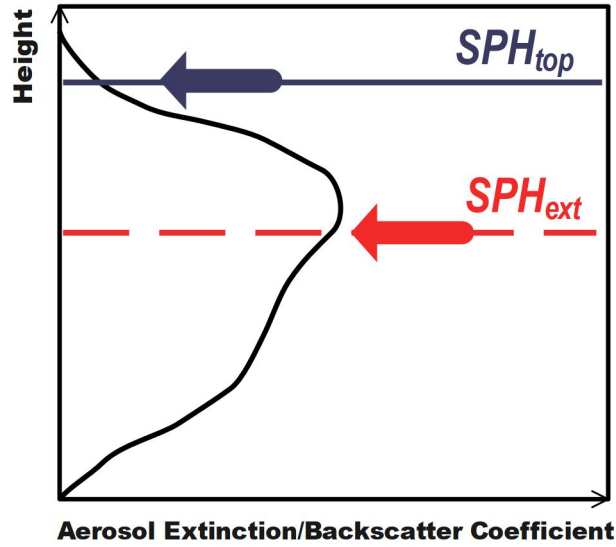
Figure 2: Schematic of two standard *SPH* definitions, *SPH_{top}* and *SPH_{ext}*, proposed in our study.

3.1.1 Plume top ($SPH_{top}$$SPH^{top}$)

This definition is built on the wavelet covariance transform (WCT) approach given by Gamage and Hagelberg (1993), which is an

280   automatic algorithmic process to extract geometrical features of interest. Since it can detect the aerosol layer locations of subtle but coherent transitions according to their strength and sign, the WCT analysis has been applied to detect realistic high-resolution atmospheric structures at a variety of vertical spatial scales, such as a well-mixed convective boundary layer top (e.g., Brooks, 2003; Baars et al., 2008) and the edges of lofted aerosol layers (e.g., Davis et al., 2000; Siomos et al., 2017). Here we only focus on the derivation of for the top height of the of wildfire smoke plume tops for wildfire, referred to as $SPH_{top}$$SPH^{top}$.

285   The WCT method is expressed as

$$W_f(a,b) = a^{-1} \int_{z_b}^{z_t} f(z) h\left(\frac{z-b}{a}\right) dz, \qquad\qquad (1)$$

with a step function, the so-called Haar wavelet $h_{a,b}(z)$, which can be defined as

$$h\left(\frac{z-b}{a}\right) = \begin{cases} +1: b - \dfrac{a}{2} \leq z \leq b \\ -1: b \leq z \leq b + \dfrac{a}{2} \\ \;\;0: \quad elsewhere. \end{cases} \qquad\qquad (2)$$

In **Eq. (1)**, $f(z)$ is the lidar signal of interest as a function of height AGL, z (is in our case the aerosol extinction profile $\beta(z)$ at

290   355 nm), and z_t and z_b are the upper and lower limits of the profile. For any arbitrary element of the Haar basis $h_{a,b}(z)$ as shown in **Eq. (2)**, a is the dilation parameter in relation to the spatial spectrum of the function, and b is the translation parameter indicating the location at which the function is centered, respectively.

The local match or similarity between the Haar wavelet $h_{a,b}(z)$ and the lidar extinction signal $\beta(z)$ is measured in the covariance

transform $W_f(a, b)$, which can be interpreted as a pattern search for a sudden jump. Accordingly, the position of the local maxima (i.e., positive peaks) in the return WCT signal approximately marks the layer top; likewise, the position of the local minima (i.e., negative peaks) of the covariance transform $W_f(a, b)$ roughly coincides with the layer bottom. I~~To put it in another way, the i~~dentification of strong variations in the vertical gradient of the aerosol extinction profile $\beta(z)$ is useful ~~to~~ for locat~~e~~ing the boundaries between aerosol layers. Inspired by Michailidis et al. (2021, 2023), we ~~report the correct location of~~define SPH_{top}~~SPH^{top}~~ ~~by adopting~~as the last positive peak in the corresponding WCT profile from the surface to the upper atmosphere if some physical~~-related~~ constraints are satisfied. The optimum value for a affects the number of sufficiently thick aerosol layers that can be retrieved successfully. We therefore limit~~ed~~ the minimum acceptable wavelet dilation a to be equal to 54 times the vertical resolution of the aerosol extinction profile $\beta(z)$ at 355 nm, i.e., a = 162 m ~~used~~ in this study. To filter noise in the return WCT signal, a minimum threshold value is set to 0.05. The values of SPH_{top}~~SPH^{top}~~ are ~~clearly~~ extracted using this approach for both~~ for a~~ single-layer~~ed~~ and multi-layer~~ed~~ aerosol structure smoke plumes, ~~ as illustrated in **Figs. S1** and **S2**, respectively.

3.1.2 Extinction-weighted mean plume height (SPH_{ext}~~SPH^{ext}~~)

Given an aerosol extinction coefficient profile $\beta(z)$ with n lidar vertical levels, this definition weighs each height AGL interval z_i (in our case z_i=3 m) for the i-th level with the height-dependent extinction coefficient $\beta(z_i)$ as described in Koffi et al. (2012), and then calculates the weighted mean height (i.e., SPH_{ext}~~SPH^{ext}~~) as follows:

$$SPH^{ext} = \frac{\sum_{i=1}^{n} \beta(z_i) \cdot z_i}{\sum_{i=1}^{n} \beta(z_i)}.$$ (3)

The ~~above derivation~~method (**Eq. (3)**) has been widely applied in previous literature and considered ideal for comparisons with the ALH retrieval from passive satellite sensors (Chimot et al., 2018; Kylling et al., 2018; Liu et al., 2019b; Nanda et al., 2020), since it offers a simple and useful means to represent the aerosol vertical distribution as a single height value. For example, in some cases where a single and homogenous (i.e., same particle size and optical properties) aerosol layer is found in the atmosphere, SPH_{ext}~~SPH^{ext}~~ indicates ~~gives an indication of~~ the aerosol layer~~'s~~ center of mass. However, when it comes to a ~~complicated~~ vertical structure ~~of~~with multilayer aerosols, SPH_{ext}~~SPH^{ext}~~ may be ~~observed~~ at a vertical level with minimal smoke aerosol loading because smoke plumes are ~~present~~ spread out at multiple heights.

3.2 Lidar~~—~~satellite collocation method

When comparing satellite products with observations, a method to collocate the two datasets is required. Even at close range ~~to the source~~ and within ~~a~~short ~~amount of time~~periods, the vertical extent of wildfire smoke plumes can vary substantially. This variation is influenced by factors such as ~~is because~~ specific vegetation types and fuel structures, terrain characteristics, or ambient meteorological conditions, ~~during atmospheric transport processes~~ which are more favorable to aerosol aging mechanisms and plume rise behaviors than others (Paugam et al., 2016; Junghenn Noyes et al., 2022). Passive satellite remote sensing of wildfire SPH ~~provides an~~indirectly measures ~~of~~columnar quantities at a relatively coarse spatial resolution, representing the spatial average of a highly variable pixel area of fire activity and ~~therefore~~ smoke plume behavior. In contrast, a~~A~~ctive airborne lidar ~~instead~~ collects instantaneous vertical segments of smoke aerosols only along its flight path, which in turn lacks large-scale spatial representation. Along with the spatial misalignment of collocated pairs, ~~This fact precludes any perfect match between aircraft observations and satellite retrievals. T~~the disparity in sampling time between airplanes and satellites for the same cluster of wildfire plumes, on the order of minutes to days, presents another inherent challenge and thus yields few perfectly matched pairs. Hence, t~~To~~ make ~~proper~~comparisons between space- and aircraft-based observing platforms, ~~much deliberation is required in~~ determining

330 the time interval and ~~the~~ distance for collocation pairs of satellite retrievals~~observations~~ and lidar measurements requires careful consideration (Junghenn Noyes et al., 2020).

~~In our study, airborne lidar measurements are integrated to an along-track spatial resolution of about 1.1 km and thoroughly cloud-screened. Broadly, w~~We ~~come up~~developed and tested ~~with~~ two methods to collocate our aircraft observations with four satellite products (**Fig. 3**). We expect the collocation method to impact the results because of the spatial heterogeneity of smoke plumes

335 and the range of horizontal resolution for the four satellite products, from 1 km to 6 km. ~~in connection with the spatial statistics of the satellite *SPH* data. Moreover, there's a chance that~~ Another factor is that multiple satellite pixels can coexist in proximity to a single lidar point when satellite orbits and flight legs intersect. When considering these factors, using a single satellite pixel versus an average of pixels in a specific area to collocate satellite products with aircraft observations provides different results for the comparison. Testing the two methods ensures that our comparisons are fair and consistent across the different satellite products.

340 One,~~-~~ the "spatial averaging method", uses~~ing~~ an average of the surrounding satellite pixels of a lidar point, ~~(hereinafter called the "spatial averaging method")~~ and ~~another~~ the other, the "matched pair method", employs~~using~~ a nearest neighbor search to create a matched ~~pair of~~ lidar~~-~~-satellite ~~observations~~ pair~~(hereinafter called the "matched pair method")~~.
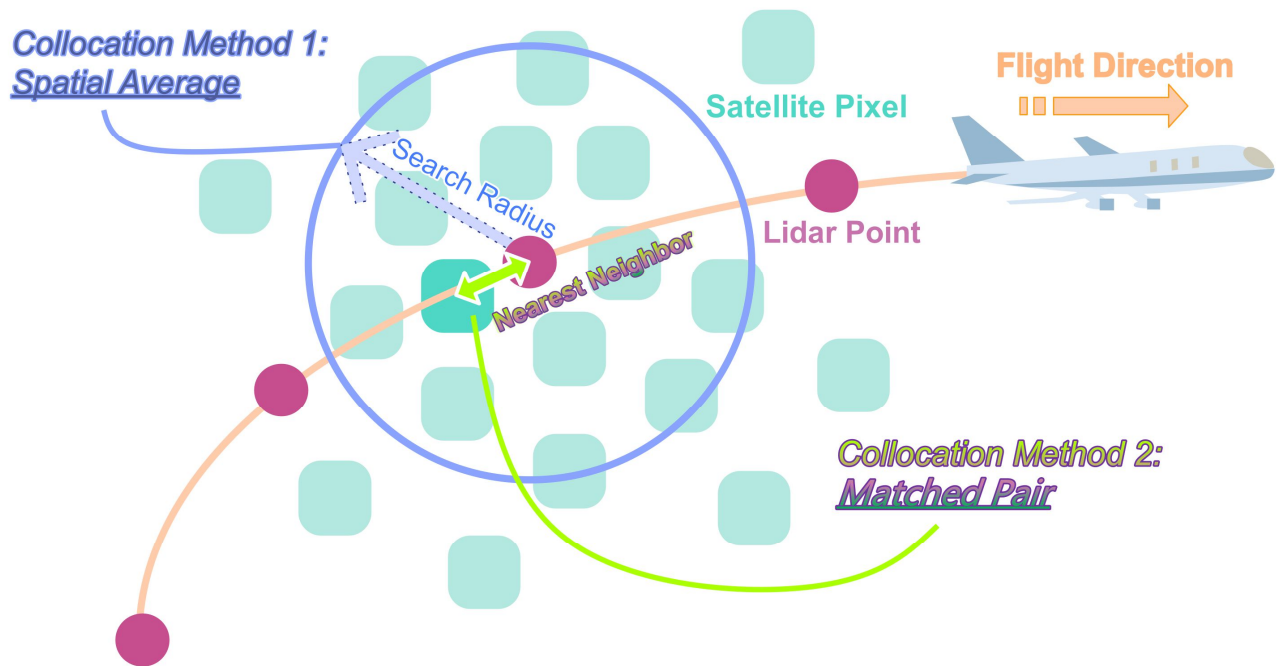
Figure 3: Conceptual diagram of two collocation methods used in our study to pair aircraft observations and passive satellite retrievals.
345 **Our collocation criteria are a search radius of 6 km and a sampling time window of 12 minutes.**

The ~~first collocation method, i.e., the~~ spatial averaging method~~,~~ calculates an average~~ed~~ value of the satellite retrievals within an area of a fixed search radius around the lidar measurement. For MODIS/MAIAC and MISR/MERLIN, since they have ~~the finest~~ finer spatial resolution (~~described in~~ **Table 1**), ~~it~~ this predisposes them to have multiple collocations inside a circular area of a given search radius centered on the lidar point. The ~~nature of their noise is~~values are smoothed ~~by taking~~because an ~~the~~ average

350 value of all satellite retrievals in this circular area for a given sampling time is used for comparison, which is a common practice in the remote sensing field (e.g., Virtanen et al., 2018). ~~Also, c~~Considering that there are fewer collocated satellite retrievals ~~of~~for the coarse resolution products~~ within the search area~~, such as VIIRS/ASHE and TROPOMI/ALH, within the search area we apply our second collocation method, i.e., the matched pair method. This method is more sensitive to the location of a single satellite

pixel coinciding with each point-like airborne lidar measurement. The closest satellite pixel to the nearby lidar point within the given sampling distance and time window is chosen for each match. ~~-~~ While using two methods provides the most reliable approach to compare across multiple satellite products, there are still uncertainties associated with satellite-observation comparisons. The main uncertainty sources of collocation mismatch ~~uncertainties~~ are~~:~~ (1) misalignment between the satellite pixel size and the lidar observation point; (2) wind-driven advection (e.g., a high fire-induced horizontal wind can reach the maximum value of 10 m s^{-1} (Liu et al., 2019c), which can displace fire-related smoke aerosols 3.6 km in 6 minutes); (3) intrinsic positioning and navigation errors. For both methods, we ~~first~~ assume that horizontal changes in wildfire smoke plume spread area are negligible during short time intervals. It is important to note that each satellite product maintains its native resolution rather than being resampled to a uniform grid for all products. A different collocation method for each satellite product might be used to showcase its spatial characteristics (e.g., to highlight the improvement of finer spatial resolution products).

Both collocation methods require spatiotemporal averaging windows to be selected. A single granule of the~~Amongst all the satellite-derived *SPH* products as discussed above, the~~ VIIRS/ASHE product has the largest pixel size (6 km × 6 km) ~~across~~ with the longest ~~period~~orbit segment scanning period (~~a nominal temporal duration of~~~ 6 minutes) of all the satellite-derived *SPH* products in **Table 1**. ~~T~~Hence, ~~t~~to ensure that adequate collocation pairs are available within one half hour due to rapid ~~in response to high-level~~ wildfire smoke plume activity, we ~~decide to use~~utilized a sampling time window of 12 minutes that corresponds to twice the maximum time span of an orbital swath (one scene)~~ in the multi-sensor satellite data~~. To investigate the effects of ~~the~~ search radius size for the two collocation methods, we used 20 sampling distances ranging from 1 km to 20 km. ~~for the radius of the circular region, by a~~Assuming a worst-case windy environment of 30 m s^{-1}~~,~~~~which results in~~ wildfire smoke aerosol layers could ~~migrating~~migrate ~20 km during the maximum allowed time-interval ~~between observations~~ of 12 minutes~~in our coincidence criteria~~. Local *SPH* spatial variability over scales up to ~20 km can introduce uncertainty in *SPH* comparisons. In **Fig. S3**~~Accordingly~~, the standard deviation (*STD*) of the multi-sensor satellite *SPH* retrievals around a lidar point (denoted by σ_{SPH}) is calculated ~~and plotted in **Fig. S3**~~ to assess the representativeness of~~-~~ the search radius~~not only the point-like lidar observation for the search area covered by the satellite data using the spatially averaging method but also the closest satellite value within the selected spatial criteria using the matched-pair method~~. With increasing distances, all *STD* curves for the satellite--retrieved *SPH* display asymptotic behavior. These values can be interpreted as an upper limit of the *SPH* errors owing to our method of collocation. It is important to optimize the inclusion criteria for the lidar-satellite comparison. For example, a low number of nearby satellite pixel counts shows higher spatial sampling uncertainty, and a low number of one-to-one collocation pairs indicates weaker statistics in calculating the *STD*. ~~While calculating~~Using the mean *STD* (~~,~~ $\overline{\sigma_{SPH}}$) from all collocations, ~~-~~the average number of nearby satellite pixels within a searc~~hing~~ radius per collocation, ~~-~~and the total number of one-to-one collocation pairs~~,~~~~are also recorded and can be used as thresholds.~~ ~~t~~The best search radius is thus set to 6 km. ~~A~~The collocated satellite *SPH* value is assumed to ~~can be taken to~~ be ~~generally~~ representative across the ~~of *SPH* values of all other observations within a~~ 6 km radius circle centered around the WCL data point, with an average *STD*-calculated uncertainty ($\overline{\sigma_{SPH}}$) of ~220 m for MODIS-Terra/MAIAC, ~173 m for MAIAC-Aqua/MAIAC, ~258 m for MISR/MERLIN, ~300 m for VIIRS/ASHE, and ~152 m for TROPOMI/ALH.

3.3 Reconstructed lidar vertical cross-sections

~~During~~ When the UWKA flew ~~flight legs~~close-to--perpendicular to the mean wind direction, the consecutive UWKA transects sampled~~s~~ the ~~fire~~ smoke plumes ~~along nearly the same flight track, albeit~~at different heights over the same latitude or longitude range of the flight trajectory. The UWKA operates at a cruise speed of approximately 90 m s^{-1}, enabling it to capture data from different altitudes and angles. ~~As mentioned earlier,~~ ~~T~~the WCL system uses laser beams to measure the optical properties of the

plume, ~~but we recognize that WCL~~and is limited in its ability to penetrate and sample ~~dense~~ optically thick smoke. Therefore, the ~~lidar~~WCL at each flight leg can only provide a partial vertical segment of the ~~fire~~ smoke plume~~s'~~ cross-section, particularly from the lowest flight altitude (i.e., upward scanning lidar).

395 We reconstruct~~ed~~ the vertical structure of wildfire smoke plumes using consecutive WCL transects from different flight legs. This post-processing approach, using pseudo-vertical profiles of the aerosol extinction coefficient ~~presents a more comprehensive view of pseudo-vertical profiles of the aerosol extinction coefficient~~, ~~and thus~~ provides ~~valuable~~ useful ~~reference~~ lidar-determined *SPH* ~~reference~~ data for ~~robust analysis~~comparison with satellite *SPH* products. The reconstruction process involves several key steps following Deng et al. (2022b):

400   I.   Applying extinction coefficient threshold: Cloud-screened WCL transects are collected from eleven flight tracks with valid collocation pairs. To separate densely localized fresh smoke from the aged background smoke, an extinction coefficient threshold of 0.1 km^{-1} is applied. This step helps remove background noise and signal attenuation in the WCL data and ensures a clear distinction between different smoke components.

     II.   Manual identification of flight legs sampling the same fire smoke plumes: ~~W~~we examine ~~select~~ flight ~~legs~~track
405   maps and locate areas where multiple flight legs intersected with a smoke plume ~~sampling~~ from the same fire ~~plumes~~source~~, by examining flight track maps and locating the areas where multiple flight legs intersected with the fire plumes~~.

     III.   Interpolating discontinuous flight segments to a complete vertical cross-section: ~~T~~to display the vertical cross-section of the smoke plume ~~s~~more smoothly and ~~to~~ aid further analysis and interpretation, scattered lidar points with
410   ~~extra~~ 2D vertical structure information from ~~various~~ multiple flight legs are interpolated to form a continuous line. The interpolation process relies on the fact that the change in latitude or longitude of the flight track~~s~~ is monotonic.

4 Results and discussion

4.~~3~~1 ~~Quantitative e~~Evaluation of satellite-derived *SPH* ~~interpreted from~~using airborne lidar *SPH*~~data~~

The comparison of satellite-based *SPH* with two distinctive *SPH* definitions ~~determined by~~using WCL data poses the following
415 question: ~~w~~What other factors ~~must be considered~~influence the *SPH* comparison? To address this question, we ~~specifically analyze~~considered two factors, distance from the fire and aerosol loading. Specifically, we defined four categories, ~~such as~~ "near-fire-event region (distance from the fire source < 20 km)" or "downwind region (distance from the fire source > 20 km)", and "~~low AOD~~AOD < 1" ~~(AOD < 1)~~ or "AOD $\geq$ 1~~high AOD~~" ~~(AOD > 1)~~. We then investigated the relationship between these factors and the *SPH* comparison for each satellite dataset (**Fig. ~~6~~4**).

420 For MODIS-Terra/MAIAC, *SPH$_{ext}$SPH^{ext}* is a better comparison than *SPH$_{top}$*~~can effectively interpret~~ for a majority of retrievals not only for the near-fire-event region but also for the downwind region, and ~~all~~the use of ~~-~~*SPH$_{ext}$* ~~are~~is not sensitive to significant variability in aerosol loading. Furthermore, the MAIAC PIH algorithm underestimates *SPH* with increasing AOD in the downwind region. Instead, for MODIS-Aqua/MAIAC, the retrievals ~~are generally highly biased~~have a high degree of bias compared to lidar-derived *SPH*, with only a few points falling within the region between the 1:1 and 1:2 lines. ~~In other words, t~~The MODIS-
425 Aqua/MAIAC ~~data~~retrievals exhibit~~s relatively~~ more consistency with the definition of *SPH$_{ext}$SPH^{ext}* near the fire source ~~during~~under high-AOD conditions (when AOD $\geq$~~>~~ 1). ~~In terms of~~The MISR/MERLIN product ~~, a fair~~has a good agreement ~~is observed~~ between the retrievals and ~~the definition of~~ *SPH$_{top}$SPH^{top}* for the areas ~~both~~ in the fire vicinity ~~of fire~~ and ~~far~~ downwind

from the fire, with outliers potentially arising fromfor thin plumes (for small lower AOD < 0.8), potentially due to the having unclear boundaries of the smoke plume near the fire source. This is because the MISR-based automated stereoscopic image requires distinct plume-like features to provide the complete vertical profile of the smoke plume. The VIIRS/ASHE product matchescompares better with $SPH_{top}SPH^{top}$ other than $SPH_{ext}SPH^{ext}$. Another interesting finding is that irrespective of AOD values, the ASHE algorithm tends to overestimate *SPH* for the near-fire-event region, while underestimating *SPH* for the downwind region. LikewiseSimilarly, the TROPOMI/ALH product displayshas lower *SPH* values far away from thefor the downwind region fire but higher *SPH* onesvalues when close to the fire, regardless of the chosen *SPH* definition and AOD conditions. The definition of $SPH_{top}SPH^{top}$ proves useful to evaluate the TROPOMI/ALH data within the near-fire-event region if the large outliers were removed, whereas the use of $SPH_{ext}SPH^{ext}$ is more appropriate for the downwind region if the outliers were removed.

TOverall, this qualitative analysis sheds light on the factors influencing the comparison between satellite-derived *SPH* and lidar-determined *SPH* definitions. These findings can aid in refining the comprehension and interpretation of *SPH* dataproducts collected from variousmultiple satellite datasets. Additionally, the physical interpretation of the potential biases in the satellite *SPH* algorithms can help design future field campaigns that provide data sets for evaluation and algorithm development. While the qualitative analysis is useful to understand the physical processes impacting the results, we also provided a quantitative evaluation of the satellite *SPH* products using the metrics described in **Appendix A** (results shown plots in **Fig. 4**).
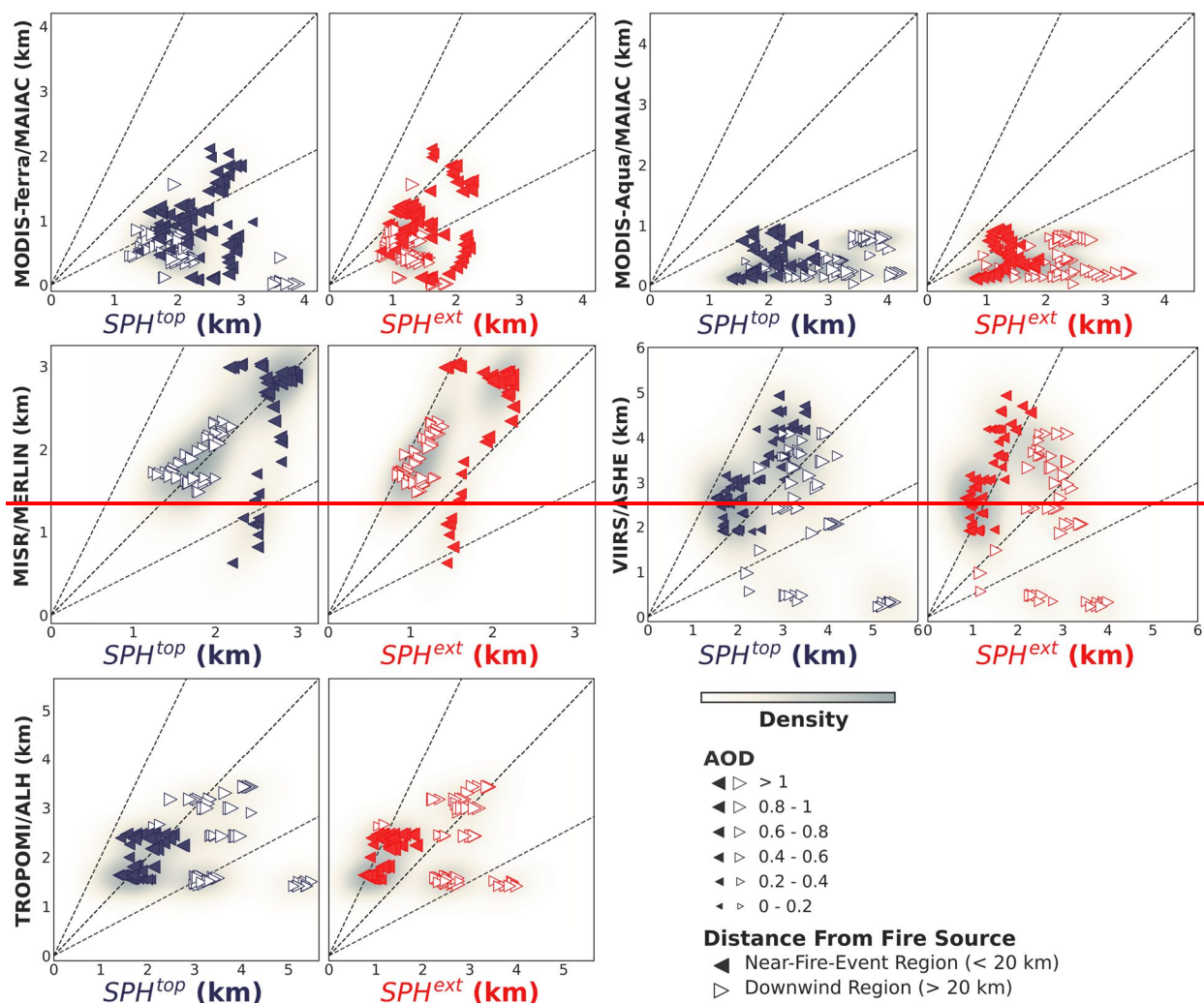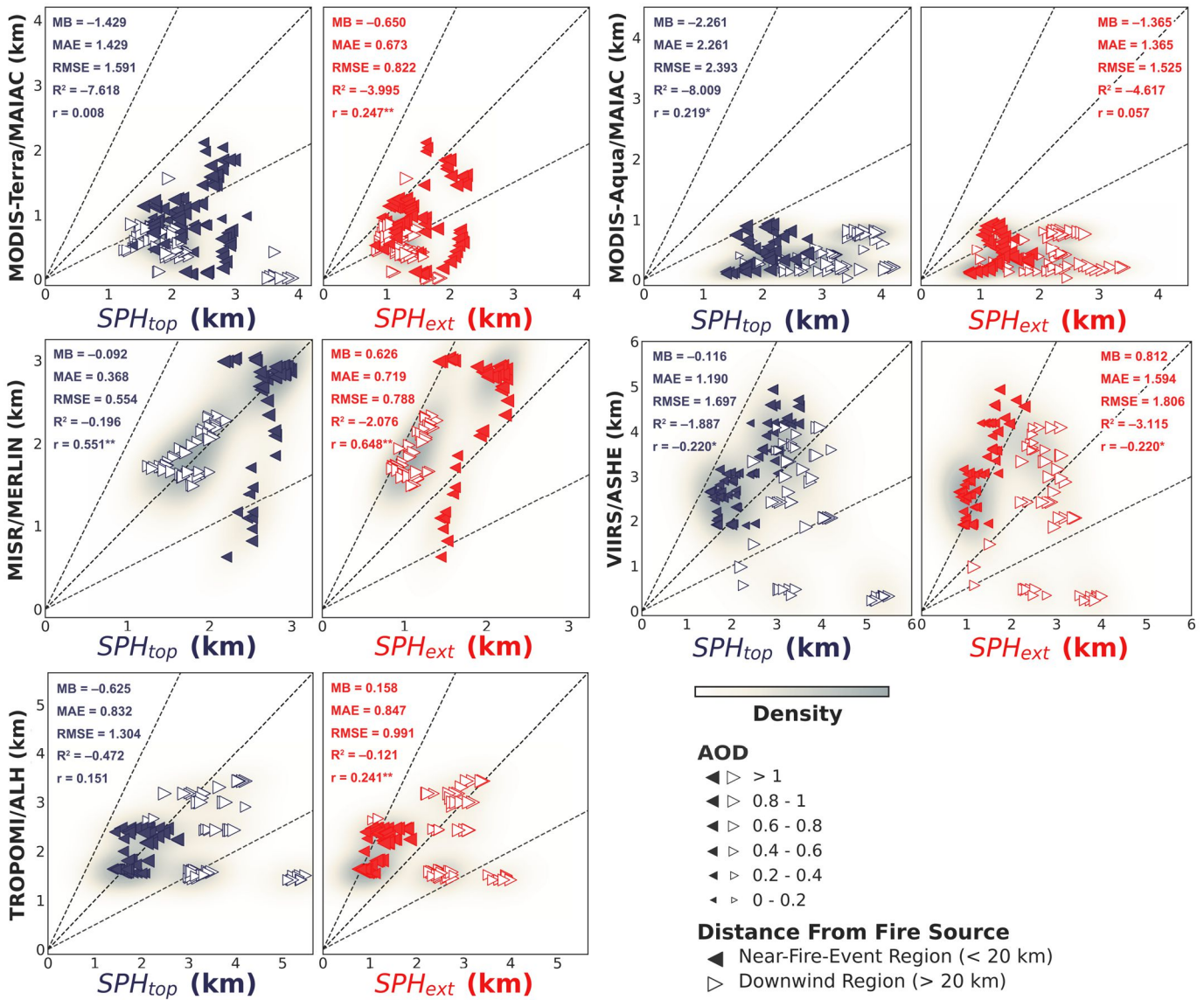
445 **Figure 6̶4: Scatterplots of satellite *SPH* retrievals from MODIS-Terra/MAIAC, MODIS-Aqua/MAIAC, MISR/MERLIN, VIIRS/ASHE, and TROPOMI/ALH versus t̶h̶e̶ WCL-determined *SPH* using two different definitions, ̶i̶.̶e̶.̶,̶: $SPH_{top}$$S̶P̶H̶^{̶t̶o̶p̶}̶$ (left, blue) and $SPH_{ext}$$S̶P̶H̶^{̶e̶x̶t̶}̶$ (right, red). Results are,̶ for the total collocated lidar–satellite pairs b̶e̶t̶w̶e̶e̶n̶ ̶s̶a̶t̶e̶l̶l̶i̶t̶e̶ ̶r̶e̶t̶r̶i̶e̶v̶a̶l̶s̶ ̶a̶n̶d̶ ̶l̶i̶d̶a̶r̶ ̶o̶b̶s̶e̶r̶v̶a̶t̶i̶o̶n̶s̶ ̶f̶r̶o̶m̶ ̶t̶h̶e̶using reconstructed WCL vertical cross-section̶s i̶n̶during August 2018. Dotted lines denote the ratios of 2:1, 1:1, and 1:2 for reference. The shaded areas show the estimated density e̶s̶t̶i̶m̶a̶t̶e̶s̶ of the o̶v̶e̶r̶a̶l̶l̶ collocated pairs'̶ ̶d̶i̶s̶t̶r̶i̶b̶u̶t̶i̶o̶n̶. Points closer to the fire (̶o̶c̶c̶u̶r̶r̶e̶n̶c̶e̶,̶**
450 **within 20 km)̶,̶ are shown as left-pointing triangles, while those farther away, in the downwind area, are shown as right-pointing triangles. E̶a̶c̶h̶The triangle'̶s̶ size c̶a̶n̶ ̶b̶e̶ ̶u̶s̶e̶d̶ ̶t̶o̶ ̶i̶n̶f̶e̶r̶ ̶i̶t̶s̶ ̶m̶a̶t̶c̶h̶i̶n̶g̶denotes the corresponding AOD value. Note t̶h̶a̶t̶:̶ the subpanel p̶l̶o̶t̶ axes'̶ scales for each satellite product are different. Evaluation metrics used to assess the performance of satellite products are *MB* (km) – mean bias; *MAE* (km) – mean absolute error; *RMSE* (km) – root mean square error; R^2 (unitless) – coefficient of determination; and *r* (unitless) – Pearson correlation coefficient (* signifies a p value < 0.05, ** indicates a p value < 0.01).**

455 ~~**Table 4** summarizes the statistical evaluation for collocated pairs for wildfire *SPH* between multiple satellite products and lidar measurements, where *MB* (km) = 0, *MAE* (km) = 0, *RMSE* (km) = 0, and *r* (unitless) =1 indicate perfect agreement.~~ The ~~set of~~ evaluation metrics ~~can be~~are calculated by **Eqs. (A1)** to **(A4̶5)**, where *MB* (km) = 0, *MAE* (km) = 0, *RMSE* (km) = 0, and *r* (unitless) =1 indicate perfect agreement. The ~~resulting~~ *SPH* values used ~~to calculate~~for ~~evaluation~~ metrics are the ~~means~~averages of all successful collocations ~~using~~found in reconstructed lidar vertical cross-sections. Additional statistics for the lidar–satellite

460 comparisons are summarized in **Appendix B**. It should be noted that the collocation method used for comparison is not the same across all of satellite products, where MODIS-Terra/MAIAC, MODIS-Aqua/MAIAC, and MISR/MERLIN uses the spatial averaging method, and VIIRS/ASHE and TROPOMI/ALH uses the matched pair method. Results for both collocation methods

for all satellite products are provided in **Tables S1** and **S2**. The statistical comparisons of four *SPH* products derived from passive satellite remote sensing against WCL-determined *SPH* further elaborates on the strengths and limitations of these distinct observational methods. Next, we present an in-depth assessment of the performance of each product based on the quantitative evaluation.~~It should be noted that~~ **~~Table 4~~** ~~is the combination of~~ **~~Tables S3~~** ~~and~~ **~~S4~~**~~, using spatial averaging and matched pair methods for collocation relating to different satellite products.~~

The MAIAC PIH algorithm has low confidence (i.e., large negative R^2 from -8.009 to -3.995 and high *RMSE* from 0.822 to 2.393) in *SPH* retrievals compared to the WCL *SPH* measurements using two definitions, especially in the afternoon. One reason might be that the MAIAC algorithm cannot achieve strong negative thermal contrast, that is, the smoke pixel (white) is not enough "colder" than the background (dark) in the afternoon when the fire activity is most active. Moreover, assuming an average lapse rate over mountainous terrains instead of more accurate atmospheric temperature profiles from reanalysis data can introduce more ~~inherent~~ uncertainties in *SPH* estimates. A more significant difference between the MODIS/MAIAC *SPH* product and the definition of SPH_{top}~~SPH^{top}~~ is found compared to the definition of SPH_{ext}~~SPH^{ext}~~, indicating the limitation of high enough total AOD to ensure sufficient gaseous absorption constrains its ability to detect SPH_{top}~~SPH^{top}~~. Therefore, using~~applying~~ the definition of SPH_{ext}~~SPH^{ext}~~ to evaluate the MODIS/MAIAC product ~~would be~~is recommended.

The MISR/MERLIN ~~data~~plume height fluctuates from 0.625 km to 3.029 km, and the corresponding SPH_{top}~~SPH^{top}~~ determined ~~by~~from lidar profiles varies from 1.254 km to 2.982 km. The mean, *STD,* and quartiles of the collocated MISR/MERLIN *SPH* ~~data exhibit~~have relatively small biases compared to SPH_{top}. The MISR/MERLIN product outperforms the other three datasets for capturing SPH_{top}~~SPH^{top}~~ as seen from the lowest values of *MB*, *MAE*, and *RMSE*. It also has a ~~relatively~~ moderate positive relationship ($r = 0.551$) with the ~~spatial~~changes in ~~wildfire~~ SPH_{top}~~SPH^{top}~~. This is ~~in line with what we~~ anticipated as contrasting features are visible inside plumes and between smoke aerosols and the terrain surface through multiple, angular views, allowing the MISR stereo technique to capture the evolution of wildfire smoke plumes~~ in the cases studied~~.

Lee et al. (2015) highlighted that the VIIRS/ASHE product performs well over mountainous areas due to the surface elevation consideration during the retrieval process. Although the mean values and general distribution of both satellite retrievals and lidar observations are fairly close, the VIIRS/ASHE data has a wider spread of values (larger *STD*), a slight tendency to underestimate ~~the~~ SPH_{top}~~SPH^{top}~~ by nearly 116 m, and lower plume height extremes (maximum and minimum plume heights). A fraction within 1.5 km of 14% for VIIRS/ASHE *SPH* leads to some outliers, which are reflected in higher *MAE* and *RMSE*. These large outlier errors could be attributed to difficulties for passive sensors in measuring the presence of multi-layered aerosols (see **Figs. 7~~5~~b** and **S6d**), and a ~~potential~~potentially high AOD bias over bright surfaces. However, the negative ~~spatial~~correlation ($r = -$~~ $-$~~0.22) between the VIIRS/ASHE data and the WCL-determined *SPH* suggests significant discrepancies in their spatial resolution when collocating.

~~On~~Using the definition of SPH_{ext}~~SPH^{ext}~~, the TROPOMI/ALH product slightly overestimates *SPH* by approximately 158 m, but maintains overall reasonable performance as indicated by the *MAE* and *RMSE* values, and a weak positive correlation ($r = 0.241$) with lidar observations. However, this evaluation could be influenced by a limited number of collocations. Choosing the appropriate *SPH* definition to interpret the TROPOMI ALH algorithm depends on a case-~~-~~by-~~-~~case basis as shown in the reconstructed lidar curtains (**Sect. 4.2~~3~~**). ~~For~~When multi-layered structures are detected in the sample cases (**Fig. 7~~5~~b**), the *SPH* ~~output~~from the TROPOMI ALH algorithm is regarded as the average computation of aerosol optical properties, resulting in a poor comparison with the lidar *SPH*. On the other hand, the TROPOMI ALH algorithm shows encouraging potential for characterizing SPH_{top}~~SPH^{top}~~ in homogenous well-developed smoke layers (**Figs. S6~~4~~f** and **S6~~4~~i**). ~~When using the TROPOMI/ALH product,~~

500 ~~m~~Multilayered aerosols, inaccurate aerosol type detection, and biased UVAI retrievals over bright areas with complex terrain are all potential causes of retrieval uncertainties in the TROPOMI/ALH product.~~can increase the biases in wildfire smoke profiling.~~

Overall, the discrepancies between passive satellite retrievals and lidar measurements in observing *SPH* primarily stem from their different approaches to characterize smoke aerosol. Passive satellites typically operate under the assumption of a singular aerosol layer within the atmospheric column, a simplification that often fails to account for the presence of multiple layers that are actively

505 captured by lidars. This divergence creates a challenge in aligning satellite-derived *SPH* data with lidar observations due to the uncertainty in correlating equivalent layers. Further investigation of the smoke plume physics and vertical aerosol distributions are provided in the following sections using the WCL vertical profiles, including comparisons with passive satellite *SPH* products.

~~4.4 Qualitative evaluation of satellite-derived *SPH* and physical considerations~~

4.~~1~~2 Leveraging airborne lidar measurements to characterize plume behavior and *SPH*

510 Through the use of airborne lidar measurements, our study seeks to understand ~~Our study attempts to determine a reliable method for evaluating the effectiveness of~~how well a passive satellite remote sensing technique ~~in~~ can ~~retrieving~~ retrieve *SPH* ~~data from wildfires using airborne lidar measurements~~. ~~It is worth noting that the~~The lidar profiles allow for multiple aerosol layers to be sampled~~. However~~, unlike the conventional passive satellite aerosol height retrieval algorithm ~~assumes~~ which presumes the presence of a single, homogeneously distributed aerosol layer throughout the entire atmosphere. Despite different measurement

515 concepts when it comes to multiple layers of plumes, to ensure comparability between passive retrievals and active observations of ~~wildfire~~ smoke plume behavior ~~and~~ for ease of calculation, we emphasize the significance of an effective height parameter. The two different *SPH* definitions (**Sect. 3.1**) used to determine this parameter give an indication of the height of the wildfire smoke aerosol distribution as a single number.

520
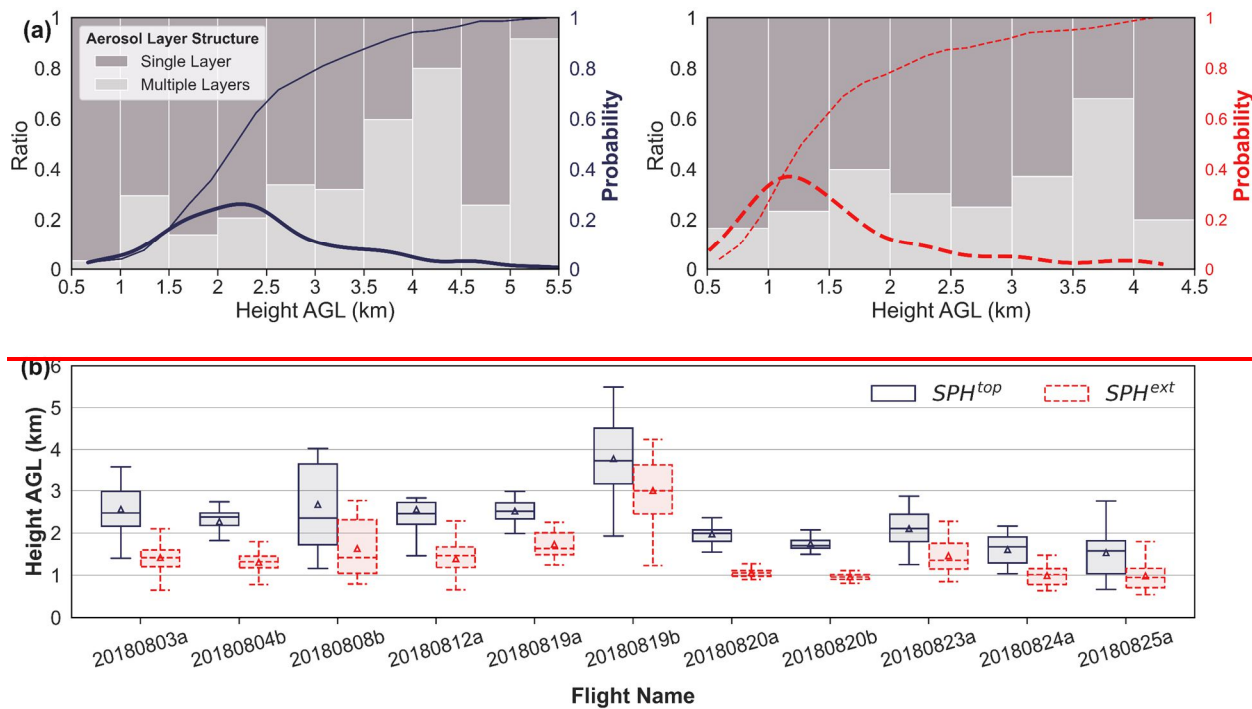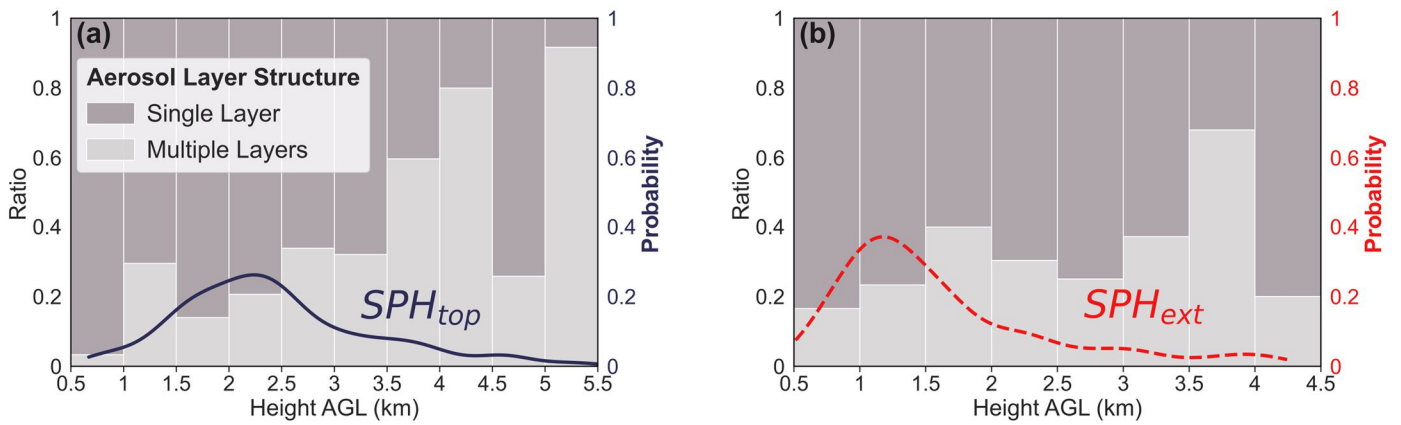
Figure 2~~5~~: ~~(a) The r~~Ratios of single-layered and multi-layered aerosol structures in the 0.5 km wide bins using two different WCL-determined *SPH* definitions: (a) ~~, i.e.,~~ *SPH~~top~~SPH^top* (left, ~~blue solid~~) ~~and (b)~~versus *SPH~~ext~~SPH^ext* ~~(right, red dotted).~~, ~~accompanied by~~Lines indicate ~~the~~ probability mass function (PMF~~; thick line) and cumulative distribution function (CDF; thin line)~~ curves. Note that the WCL plume height data are equally binned by setting the bin-width parameter to 0.5 km, and the bins are spread out in the range from 0.5 km to 5.5 km for *SPH~~top~~SPH^top* and in the range from 0.5 km to 4.5 km for *SPH~~ext~~SPH^ext*. ~~(b) WCL-determined *SPH* definition comparisons for eleven BB-FLUX flight missions presented by box plots. Upper and lower whiskers represent the 95th and 5th percentiles, respectively, while the box spans from the 25th percentile to the 75th percentile. The line inside the box represents the median (the 50th percentile), and the triangle indicates the mean of the range of plume height values.~~

In **Fig. 2a5**, the height distributions of wildfire smoke plumes ~~are shown using two different *SPH* definitions~~ during BB-FLUX in

530 August 2018 are shown using two definitions of lidar-derived *SPH*. C~~One should be c~~aution~~us should be taken when in~~identifying key criteria used to define *SPH* prior to ~~assessing~~ evaluating the satellite retrievals. This is because *SPH~~top~~SPH^top* (**Fig. 5a**) has a vertical extent spanning from 0.5 km to 5.5 km, with the most common height being approximately 2.25 km. ~~On the other hand,~~While *SPH~~ext~~SPH^ext* (**Fig. 5b**) exhibits a vertical range from 0.5 km to 4.5 km, with its peak observed at roughly 1.2 km. ~~At~~ For *SPH* values less than 3.5 km, the occurrence of smoke plumes identified within one single layer is significantly higher than

535 that of multi-layered smoke plumes (> 60% for each height bin), suggesting that the columnar *SPH* values obtained from satellite retrievals can be compared with those measured via upward-facing lidar profiles, as smoke plumes produced by wildfire typically exhibit a single aerosol layer structure. This finding holds particularly true for wildfires of decreased fire intensity under suppression operations (i.e., ~~the~~some flight dates approach~~es~~ the corresponding fire ~~contained~~ containment date listed in **Table 3~~2~~**)~~, as investigated in this study~~.

540 ~~In **Fig. 2b**, there is no clear single pattern for the vertical profile of the smoke plume due to the coupled interactions between the fire and atmosphere. Various characteristics, such as weather conditions and fuel types, can influence this relationship. Another critical factor is how far the airborne lidar is from the center of wildfire activity, which will be addressed in **Sect. 4.4**. The aforementioned results have implications for models and retrieval algorithms that presume a standard atmospheric vertical profile with a fixed temperature lapse rate and smoke concentrations. However,~~It should be noted that the upward-sampled WCL can only

545 provide a partial vertical segment and not a fully resolved cross-section of the smoke plumes from the lowest flight height due to the restricted lidar laser penetration in optically thick smoke plumes. For instance, when probing the plume centerline, there is complete attenuation of the lidar beam, resulting in a loss of data samples. However, the WCL can successfully delineate the atmosphere on each pass in the less dense portions of smoke plumes. Therefore, the vertical structure of individual smoke plumes reconstructed from airborne WCL measurements yields the vertical profiles of the mean aerosol extinction coefficient, reflecting

550 the average conditions of smoke plumes over multileg UWKA sampling periods (see more details in **Sects. 3.3** and **4.3**). In terms of lidar-derived *SPH* biases identified in our study, we observe three main scenarios: ~~the results presented here~~(1) underestimation of~~e the~~ *SPH~~top~~SPH^top* (i.e., optically thick plumes limiting vertical extent); (2)~~and~~ overestimation of~~e the~~ *SPH~~ext~~SPH^ext* (i.e., the upward-pointing lidar not sampling below aircraft); (3) underestimation of both *SPH~~top~~* and *SPH~~ext~~* in situations where the lidar

faces both dense smoke above and cannot measure below the aircraft. It should be noted that the range of WCL *SPH* measurements for both morning and afternoon flight missions on August 20, 2018, is limited because only a small fraction of flight tracks are considered valid transects for reconstruction.

Table 3: Summary of nine wildfire cases with its general information with respect to start date, approximate contained date, and approximate acres burned, which were collected from the GeoMAC (Geospatial Multi-Agency Coordination Group) historic fire dataset (last access: 8 June 2023).

Wildfire Name	Start Date	Approximate Containment Date	Approximate Acres Burned
Sharps Fire, ID	Jul 29, 2018	Aug 12, 2018	64, 812
Rabbit Foot Fire, ID	Aug 2, 2018	Sep 19, 2018	36, 031
Watson Creek Fire, OR	Aug 15, 2018	Sep 9, 2018	59, 067
Sheep Creek Fire, NV	Aug 18, 2018	Aug 23, 2018	59, 789
South Sugarloaf Fire, NV	Aug 17, 2018	Sep 3, 2018	233, 608

How smoke aerosols are vertically distributed throughout the atmosphere plays a dominant role in AOD-based surface particulate matter (PM) models. High-elevation smoke aerosol layers above the planetary boundary layer height (*PBLH*) lead to high column AOD while not elevating the near-surface PM levels. Generally, aerosol concentrations are low in the higher, relatively stable atmospheric layers above the planetary boundary layer (PBL). However, a large wildfire, usually defined as a fire area greater than 1,000 acres burning in the WUS (Linley et al., 2022), tends to have vigorous buoyant plume cores that can lift the smoke plumes to the free troposphere (FT) and even the stratosphere under favorable atmospheric conditions. Therefore, the ratio of effective *SPH* to *PBLH* (*SPH:PBLH*) is a better indicator of the AOD and surface PM concentration relationship. Now if we incorporate the modeled *PBLH* from the Weather Research and Forecasting Model (WRF) as indicated in **Fig. 3**, we can better understand local meteorology and its impact on wildfire *SPH*. The WRF model for our use has an outer domain extending over the WUS. with a 4 km spatial resolution, nudged with observations from weather stations as well as balloon soundings. *PBLH* is recalculated from the WRF simulations using the vertical potential temperature gradient method or the Richardson number method. The locations and elevations of each balloon sounding station are in **Table S1**, and details of the WRF model configuration are in **Table S2**. The results of the WRF model evaluation are in **Fig. S4**.

Based on the specific wildfire information in **Table 3**, we can qualitatively discuss the differences between $SPH^{top}:PBLH$ and $SPH^{ext}:PBLH$ for each wildfire in terms of their start dates, approximate containment dates, and approximate acres burned. The ratio *SPH:PBLH* can explain a joint interaction between buoyant plume cores and complicated boundary layer mixing (e.g., entrainment and wind shear). It also depends on other important factors such as the fire size, distance from the fire source, and the fire spread. In some cases, high $SPH^{top}:PBLH$ (> 1) but low $SPH^{ext}:PBLH$ (< 1) occur concurrently, as shown in **Fig. 3**. This means that a higher columnar AOD does not necessarily give rise to the majority of the smoke plume concentrations being above the PBL. For instance, the Watson Creek Fire that started on August 15, 2018, had two flight missions, 0819a and 0819b, and their aviation operation dates were fairly close to the fire start date compared to 0824a and 0825a. The challenging terrain with dense fuel on the ground facilitated rapid fire spread, and no containment efforts were in place. Therefore, we can expect that the intense fire behavior would generate a higher amount of smoke plumes injected into the FT, where both $SPH^{top}:PBLH$ and $SPH^{ext}:PBLH$ are larger than 1. Five days later, as the fire activity reduced and containment of the fire increased to 15%, there was likely more smoldering and thus lower plume heights. SPH^{ext} reaches a similar level to the *PBLH*, although $SPH^{top}:PBLH$ remains relatively high. When comparing the morning and afternoon *SPH* patterns, the morning *SPH* relationships might be less complex and potentially easier

590 ~~to model. Basically, turbulence, convection, and fire-atmosphere interactions contribute to more chaotic plume and PBL dynamics in the afternoon, causing the growth rate of the fire to exceed the growth rate of the PBL. The Sheep Creek Fire is an exception. It was accidentally begun by a crashed helicopter but was nearly 100% suppressed within one week, due to a timely and consistent fire response making rare *SPH* behavior in the afternoon possible, where smoke plumes reside within the PBL. Additionally, a significant portion of the lidar vertical cross-section is missing for the 0823a flight during the South Sugarloaf Fire, as depicted in **Fig. S6g**. In spite of the fire's high severity, which categorizes it as an extreme wildfire episode, the absence of the extinction coefficient data as well as lidar measurements in the downwind region (described in **Table 2**) leads to inaccurate, low estimates of SPH^{top} and SPH^{ext}.~~
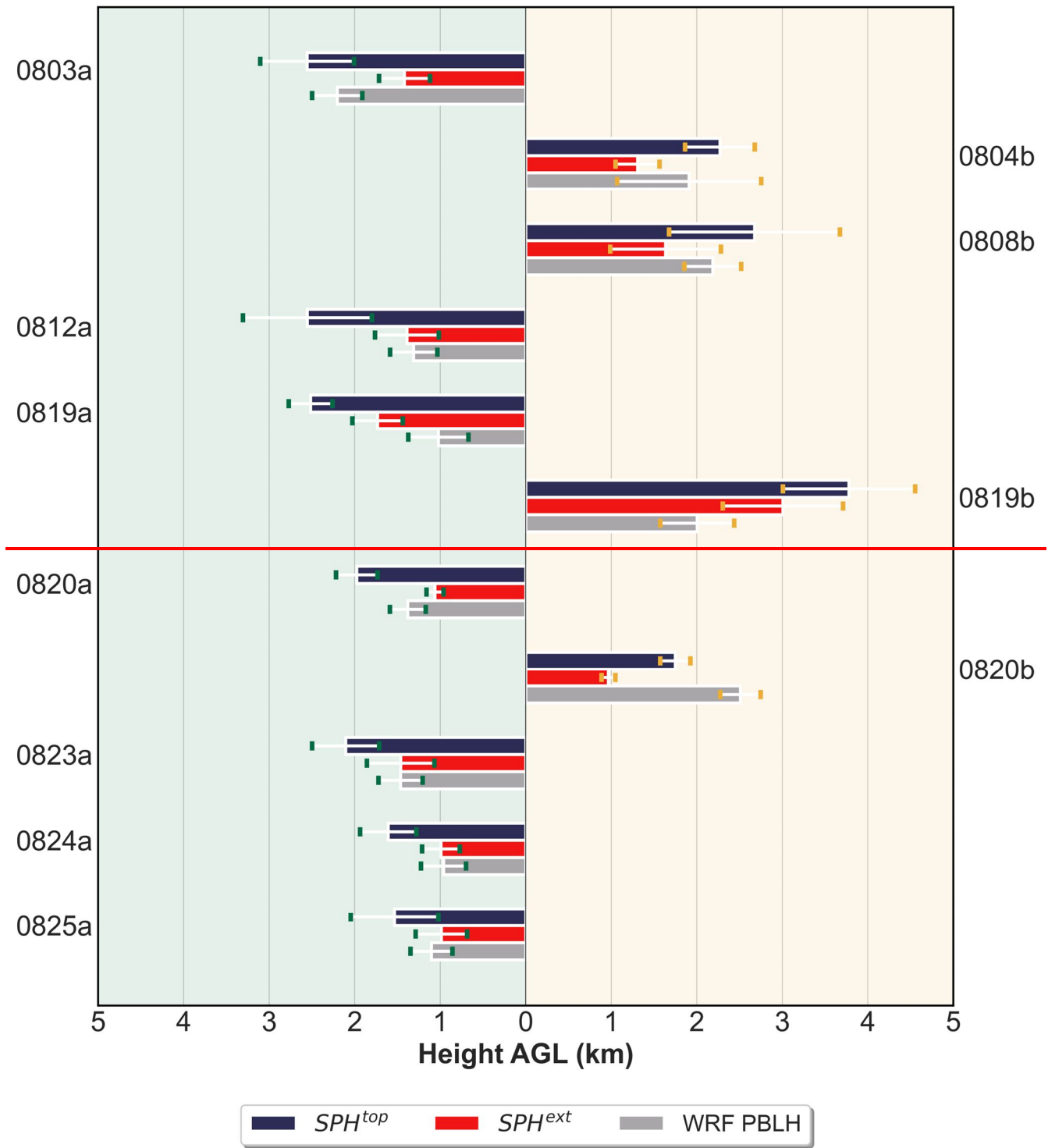
4.2 3 Reconstructed lidar curtain and lidar—satellite collocationcomparison

600   It is necessary to implement post-processing procedures to conduct a comparative analysis between the lidar observations and the satellite retrievals. Here we present detailed reconstructed lidar vertical cross-sections of aerosol extinction coefficient along with

collocated satellite *SPH* ~~data~~ on August 19, 2018, for the morning (0819a, **Fig. 6**~~4~~) and afternoon (0819b, **Fig. 7**~~5~~) flight ~~missions~~. Similar plots are included in **Figs. S4**~~5~~ and **S5**~~6~~ for each flight. **Figs. 6**~~4~~**a** and **7**~~5~~**a** demonstrate that the smoke plume coverage of the MISR/MERLIN product aligns well with the manually identified plume area and reveals high-resolution *SPH* retrievals. In contrast, the MODIS/MAIAC product with the highest spatial resolution displays lower *SPH* values in general over ~~primary~~ biomass-burning regions. Meanwhile, both the VIIRS/ASHE product and the TROPOMI/ALH product indicate that higher *SPH* values are generally shifted towards the downwind region ~~of fire sources~~.

The vertical distributions of wildfire smoke aerosols (**Figs. 6**~~4~~**b** and **7**~~5~~**b**) are useful to visualize the smoke plume structure and provide more information about the physical processes influencing aerosol layering in the atmosphere. A visual comparison of the *SPH* values from the four satellite products ~~and~~ against the WCL is presented in **Figs. 6**~~4~~**b** and **7**~~5~~**b**. In **Fig. 6**~~4~~**b**, even when faced with intricate aerosol structures, the MISR/MERLIN data is capable of reaching SPH_{top}~~SPH^{top}~~, except for thin plumes with comparably low AOD values. The MODIS-Terra/MAIAC ~~data~~ *SPH* ~~appears~~ is similar to SPH_{ext}~~SPH^{ext}~~, although it is unable to distinguish the top of multiple aerosol layers and consequently produces exceptionally low *SPH* values. Since the reconstructed aerosol vertical cross-section for **Fig. 7**~~5~~**b** is located in the downwind region ~~of the burn area~~, there is an increase in SPH_{top}~~SPH^{top}~~ and SPH_{ext}~~SPH^{ext}~~ as the distance from the fire ~~source~~ increases. We recommend caution when using the MODIS-Aqua/MAIAC product for estimating downwind *SPH*, as its effectiveness in such scenarios is not always optimal (also refer to **Figs. S4b** and **S4c** for more details). This limitation in the MAIAC PIH algorithm has also been reported in previous studies (Lyapustin et al., 2019; Loría-Salazar et al., 2021). ~~It is not advisable to use the MODIS-Aqua/MAIAC product for estimating downwind *SPH* due to its suboptimal performance in such scenarios.~~ Regarding heterogeneous aerosol vertical profiles, the spatial agreement between the collocated VIIRS/ASHE *SPH* values and the two *SPH* definitions~~' general trends~~ is poor, despite achieving, on average, a good numerical agreement with SPH_{top}~~SPH^{top}~~. This is partly due to the coarse spatial resolution of OMPS UVAI data used in the algorithm (~50 km at nadir; ~100 km near the scan edge) not being able to represent finer-scale features. The TROPOMI/ALH data ~~seems~~ is consistent with the ~~valid~~ SPH_{ext}~~SPH^{ext}~~ values, given the observed overestimation of SPH_{ext}~~SPH^{ext}~~ attributable to the elevated flight height. The potential explanation for this phenomenon is that in cases where there may be several layers of smoke aerosols, the retrieved *SPH* would be the average height of the plume much lower than the height of ~~where~~ the optically thick aerosol layer ~~is placed~~ (Michailidis et al., 2023).

According to these results and specific fires studied, the MODIS/MAIAC product struggles with most heterogeneous aerosol structures even in close proximity to active fire sources. ~~The evaluation of the MODIS/MAIAC-derived *SPH* in the afternoon is lacking in literature because MISR onboard the Terra as a comparison data set does not coincide with the Aqua overpass time in the afternoon.~~ Even though the MISR/MERLIN product aims to capture the top boundary of the smoke plume, it can be highly biased in thin plume height estimates with low AOD, ~~or~~ for a more complex aerosol structure with multiple aerosol layers. The challenges observed for the VIIRS/ASHE retrievals are: (1) poor correlation with general trends in lidar measurements; (2) it may not accurately represent complex atmospheric conditions with multiple aerosol layers. ~~Among~~ Out of the four satellite *SPH* datasets we investigated, TROPOMI/ALH has the ~~lowest~~ least ~~*SPH*~~ variance in the retrieved *SPH* across spatial areas~~., which~~ This is not ideal for ~~application purposes~~ practical use since ~~as the~~ real-world wildfire and smoke plume activity varies significantly~~-~~ in space and time~~across spatial areas~~. However, elevated smoke layers with a high aerosol loading, over dark surfaces at not very high altitudes are favorable for the TROPOMI ALH algorithm to retrieve vertically localized aerosol layers in the free troposphere.
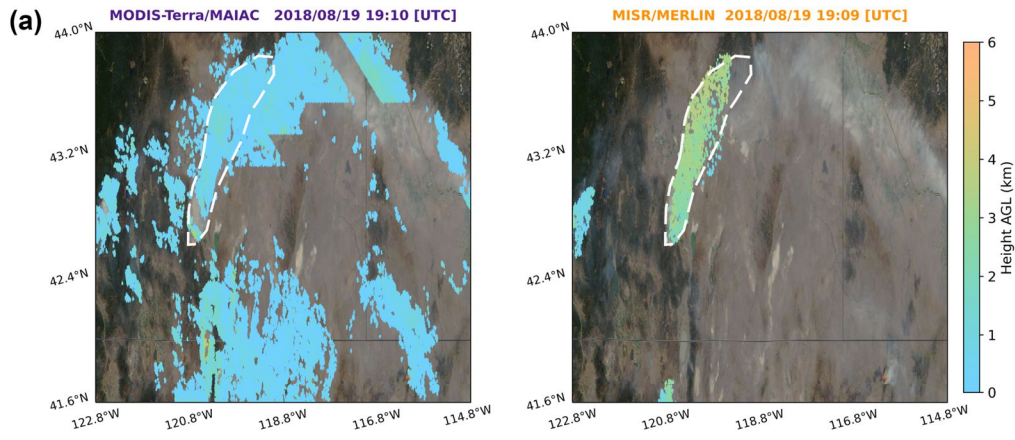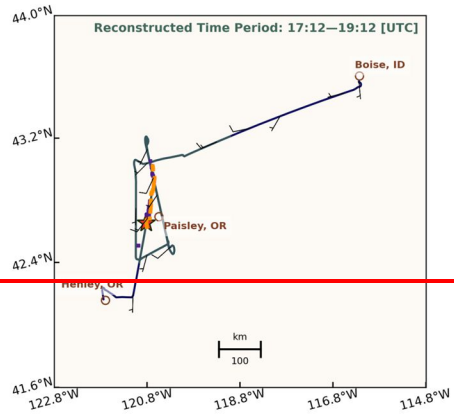
(a)
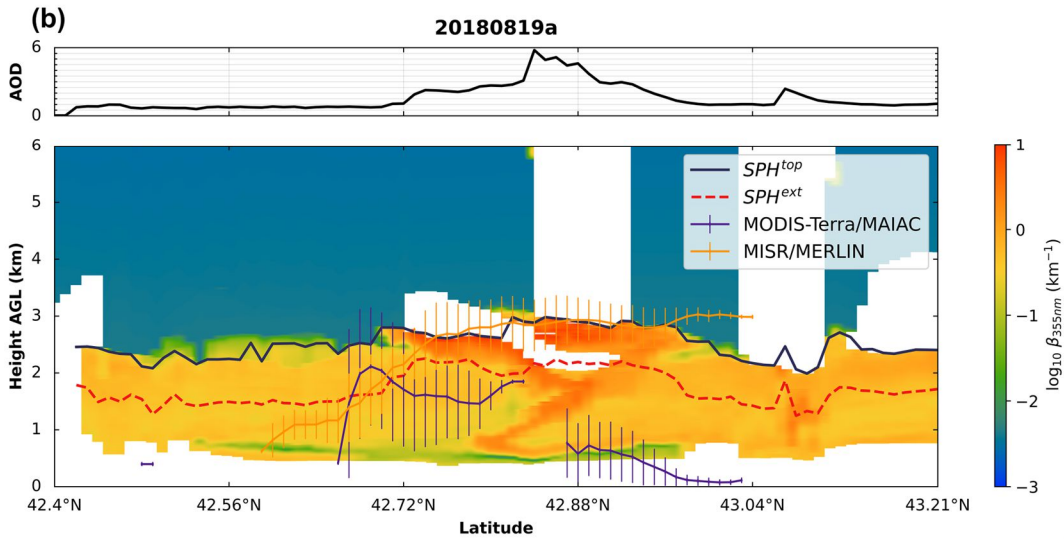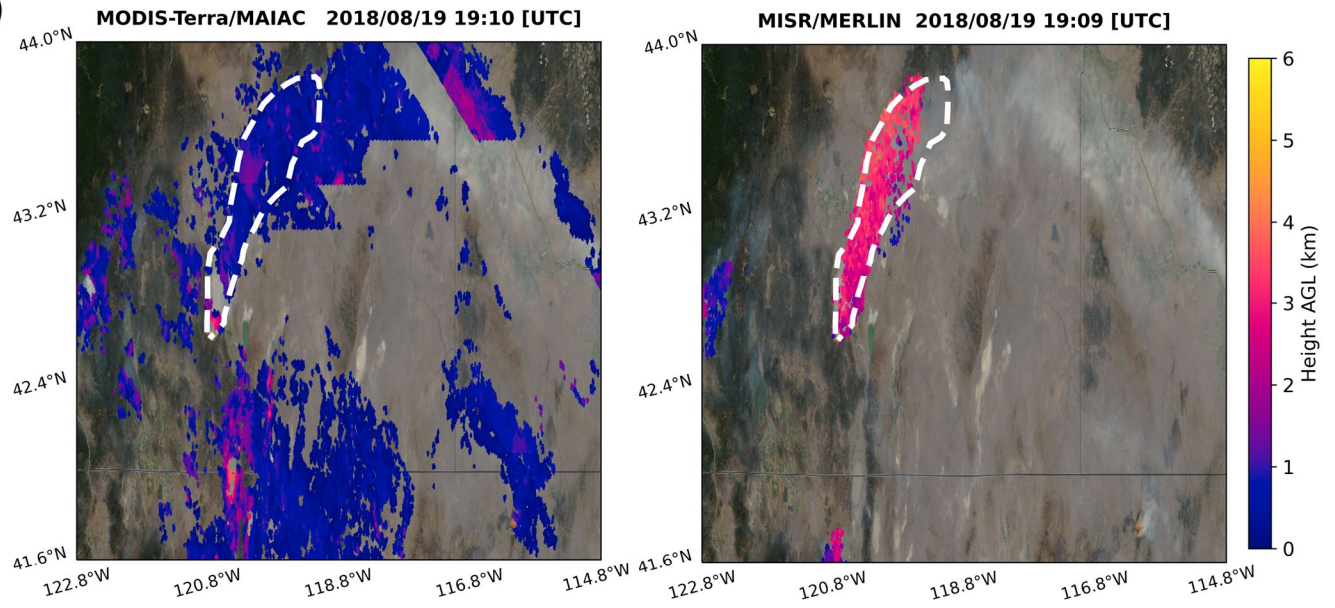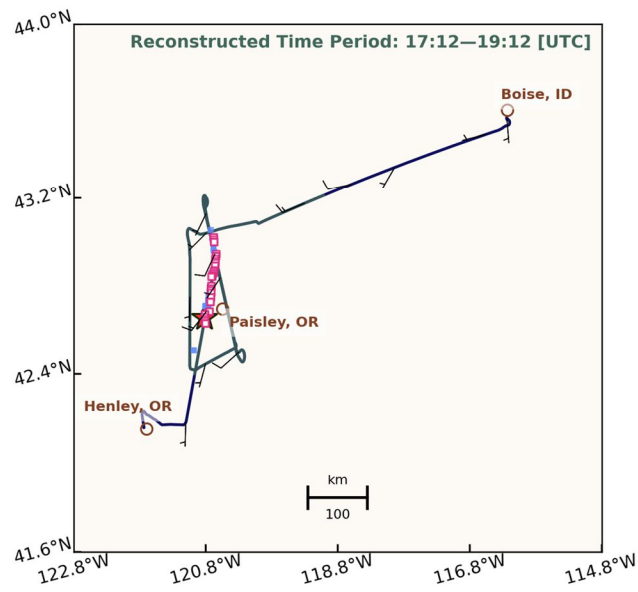
640

Figure 6: Cont.
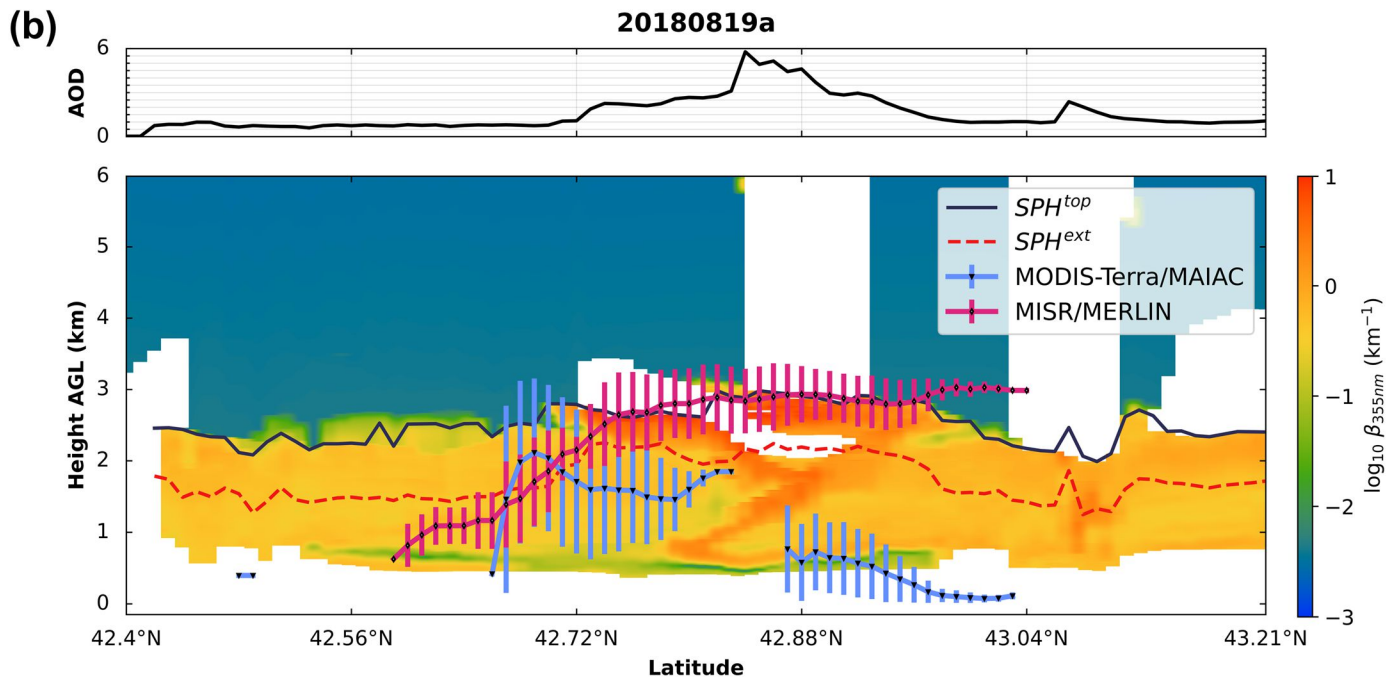
Figure 64: (a) The nearest satellite pixels ~~of (~~MODIS-Terra/MAIAC and ~~, purple,~~ MISR/MERLIN ~~; orange)~~ to the corresponding airborne lidar points along the 20180819a flight track during the reconstructed time period from 17:12 to 19:12 UTC highlighted in green. Wind barbs are plotted along the trajectory with each short barb representing 5 knots and each long barb representing 10 knots. The star symbol indicates the center location of the Watson Creek fire taken from the incident report system (Inci-Web). Note that t~~T~~he NASA WorldView MODIS Terra true-color (i.e., corrected reflectance) images are shown alongside the satellite-retrieved *SPH* maps with the user-drawn smoke plume polygons (denoted as the dashed white region). (b) ~~(Bottom panel)~~ Composite latitude—height cross-sections of the reconstructed WCL vertical aerosol extinction coefficient at 355 nm, overlaid with ~~performance comparisons for variations of~~ WCL-determined SPH_{top}~~SPH^{top}~~ and SPH_{ext}~~SPH^{ext}~~ and ~~as well as~~ the collocated satellite-retrieved mean *SPH* with error bars, ~~-~~for the Watson Creek fire in the morning on August 19, 2018 with ~~; (top panel)~~ the corresponding AOD ~~variations at 355 nm~~.

(a)
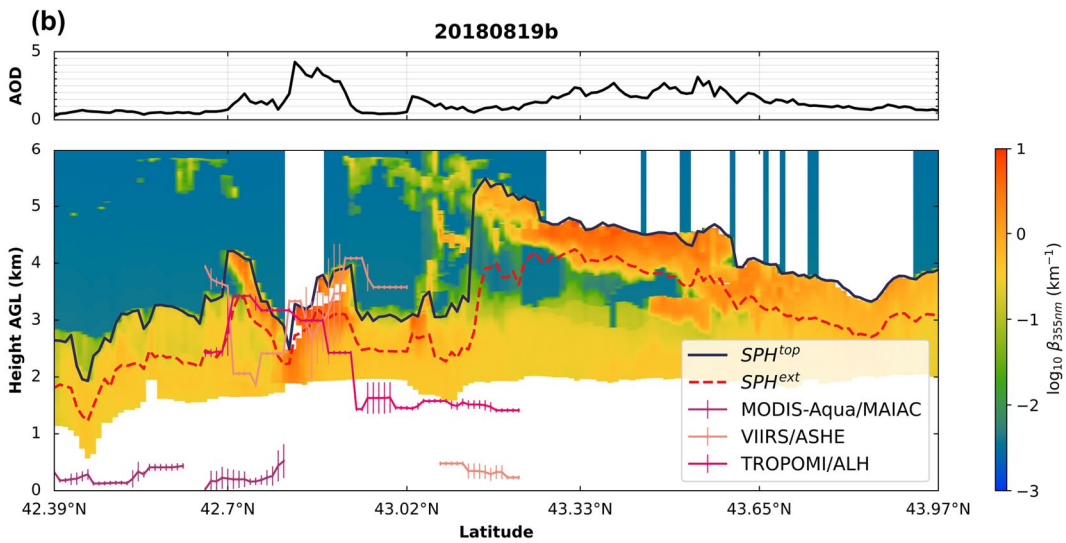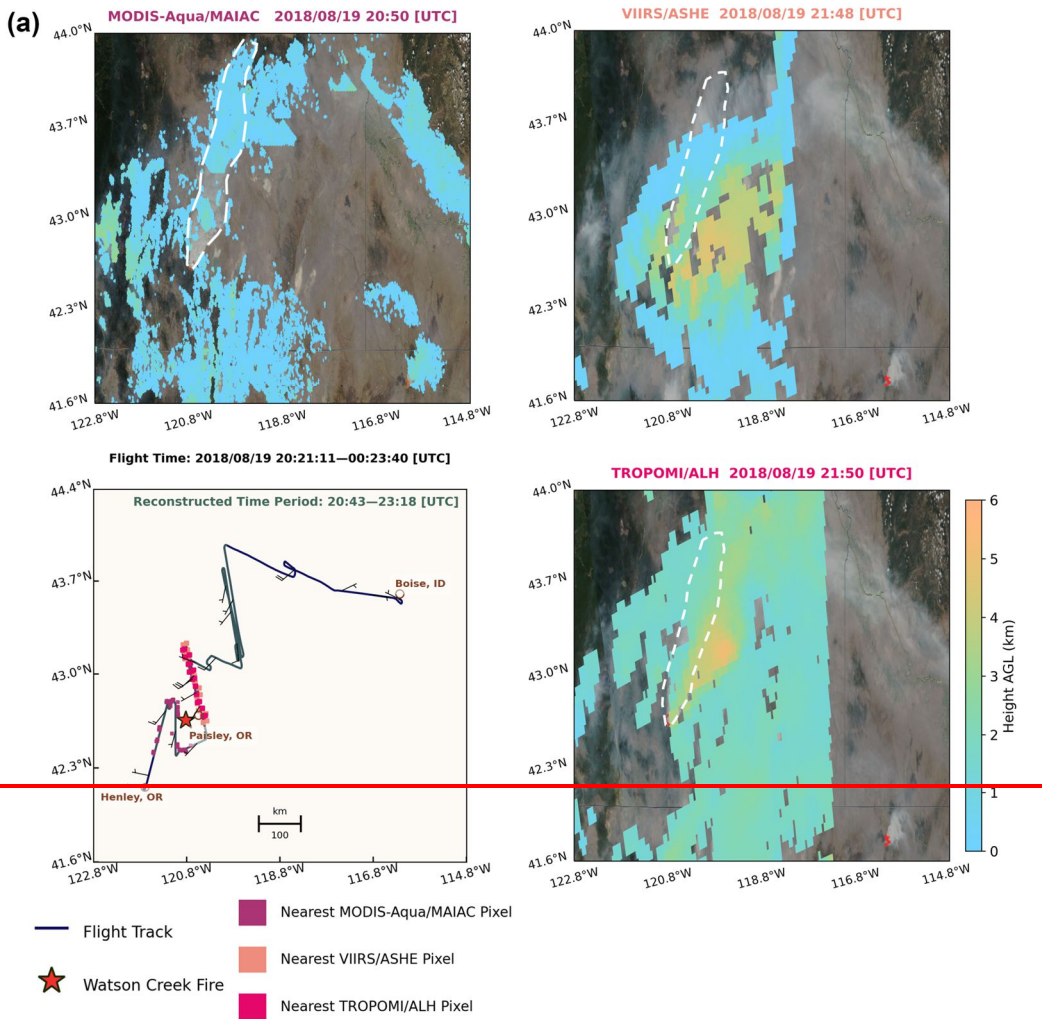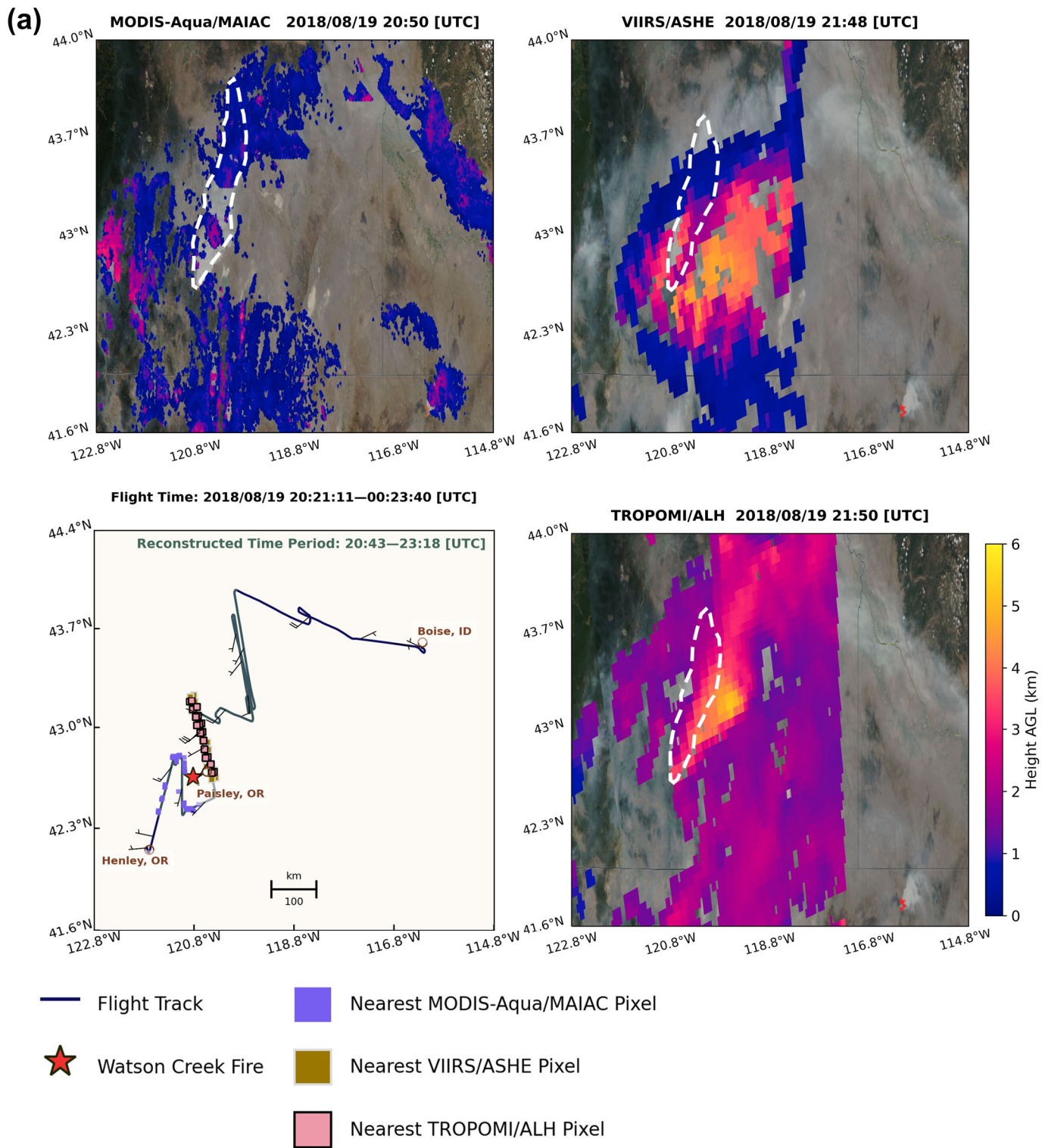
Figure 7: Cont.
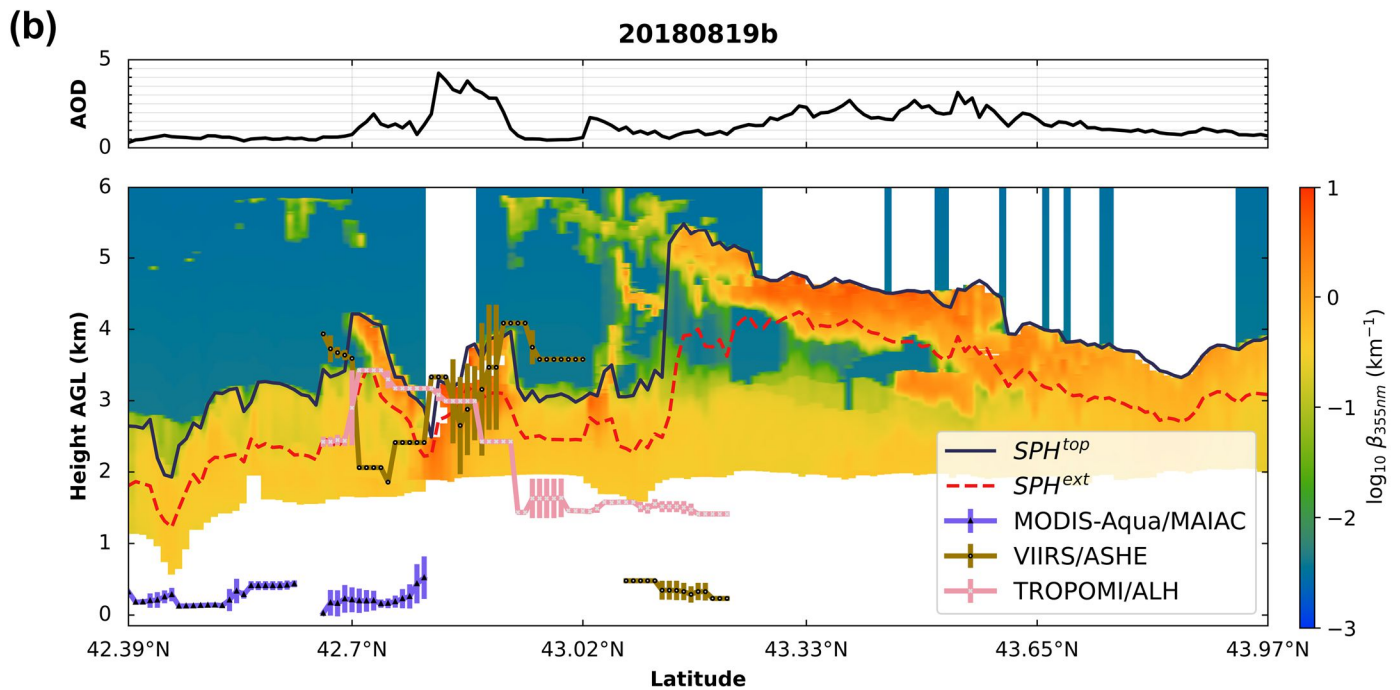
Figure ~~5~~7: (a)~~-~~ **Same as Figure 6a, but for the nearest satellite pixels of MODIS-Aqua/MAIAC, VIIRS/ASHE and TROPOMI/ALH to the corresponding airborne lidar points along the 20180819b flight track during the reconstructed time period from 20:43 to 23:18 UTC highlighted in green. Note that the NASA WorldView true-color images (both MODIS Aqua and VIIRS are used) at the corresponding moment are shown alongside the satellite-retrieved *SPH* maps with the user-drawn smoke plume polygons (denoted as the dashed white region).** ~~The nearest satellite pixels (MODIS Aqua/MAIAC, violet; VIIRS/ASHE, pink; TROPOMI/ALH, magenta) to the corresponding airborne lidar points along the 20180819a flight track during the reconstructed time period from 20:43 to 23:18 UTC highlighted in green. The star symbol indicates the center location of the Watson Creek fire taken from Inci-Web. The NASA WorldView true-color images (both MODIS Aqua and VIIRS are used) at the corresponding moment are shown alongside the satellite-retrieved *SPH* maps with the user-drawn smoke plume polygons (denoted as the dashed white region).~~ **(b) Same as Figure 6b, but for the Watson Creek fire in the afternoon on August 19, 2018.** ~~(Bottom panel) Composite latitude-height cross-sections of the reconstructed WCL vertical aerosol extinction coefficient, overlaid with performance comparisons for variations of WCL-determined *SPH^top* and *SPH^ext* as well as the collocated satellite-retrieved mean *SPH* with error bars for the Watson Creek fire in the afternoon on August 19, 2018; (top panel) the corresponding AOD variations at 355 nm.~~

4.4 *SPH* Application

Knowing *SPH* has additional benefits beyond atmospheric modeling, here we illustrate how *SPH* can be used to improve our understanding of surface air pollution concentrations and smoke plume dynamics resulting from fire–atmosphere interactions. By using both definitions of *SPH*, *SPH_top* and *SPH_ext*, additional insights related to plume dynamics can be assessed. How smoke aerosols are vertically distributed throughout the atmosphere plays a dominant role in estimating surface particulate matter (PM) models from satellite AOD products. High-elevation smoke aerosol layers above the planetary boundary layer height (*PBLH*) lead to high column AOD while not elevating the near-surface PM levels. Generally, aerosol concentrations are low in the higher, relatively stable atmospheric layers above the planetary boundary layer (PBL). However, large wildfires can have vigorous buoyant plume cores that lift the smoke plume into the free troposphere (FT) or even the stratosphere (Fromm et al., 2019) contributing to elevated aerosol concentrations above the *PBLH*. Based on burned area in **Table 2**, the fires in our study meet the definition of a megafire (10,000–100,000 ha) suggested by Linley et al. (2022), but it should be noted that fire size alone cannot characterize the fire intensity or activity and the resulting smoke plume behavior (Tedim et al., 2018). The ratio of effective *SPH* to *PBLH* (*SPH:PBLH*) is an indicator of the AOD and surface PM concentration relationship (Cheeseman et al., 2020). We incorporated the modeled *PBLH* from the Weather Research and Forecasting Model (WRF) as shown in **Fig. 8**, so we can better understand local meteorology and its impact on wildfire *SPH*. The WRF model for our use has a domain extending over the WUS with a 4 km spatial resolution, nudged with observations from weather stations as well as balloon soundings. *PBLH* were recalculated from the

WRF simulations using the vertical potential temperature gradient method or the Richardson number method (de Arruda Moreira et al., 2020). The locations and elevations of each balloon sounding station are in **Table S3**, and details of the WRF model configuration are in **Table S4**. Results of the WRF model evaluation are in **Fig. S6**.

In **Fig. 8**, there is no clear single pattern for the vertical spread of the smoke plume due to the fire–atmosphere coupling and boundary-layer turbulence (Sun et al., 2009; Deng et al., 2022b). The difference between SPH_{top} and SPH_{ext} is often greater within a single plume than the differences across different plumes. Based on the wildfire information in **Table 2**, we can qualitatively discuss the differences between SPH_{top}:$PBLH$ and SPH_{ext}:$PBLH$ for each wildfire in terms of their start dates, approximate containment dates, and approximate acres burned. SPH:$PBLH$ characterizes a joint interaction between buoyant plume cores and boundary layer mixing (e.g., entrainment and wind shear). It also depends on other important factors such as the fire size, distance from the fire source, and the fire spread. In some cases, high SPH_{top}:$PBLH$ (> 1) but low SPH_{ext}:$PBLH$ (< 1) occur concurrently, as shown in **Fig. 8**. This means that a higher columnar AOD does not necessarily give rise to the majority of the smoke plume concentrations being above the PBL. For instance, the Watson Creek Fire that started on August 15, 2018, had two flight missions, 0819a and 0819b, and their aviation operation dates were close to the fire start date, compared to 0824a and 0825a flights. The challenging terrain with dense fuel on the ground facilitated rapid fire spread, and the fire was not contained. Therefore, we can expect that the intense fire behavior would generate a higher amount of smoke plumes injected into the FT, where both SPH_{top}:$PBLH$ and SPH_{ext}:$PBLH$ are larger than 1. Five days later, as the fire activity reduced and containment of the fire increased to 15%, there was likely more smoldering and thus lower plume heights. SPH_{ext} reaches a similar level to the $PBLH$, although SPH_{top}:$PBLH$ remains relatively high. When comparing the morning and afternoon SPH patterns, the morning SPH relationships are less complex and potentially easier to model. Where turbulence, convection, and fire-atmosphere interactions contribute to more chaotic plume and PBL dynamics in the afternoon, and the growth rate of the fire exceeds the growth rate of the PBL. The Sheep Creek Fire is an exception due to a timely and consistent fire response making rare SPH behavior in the afternoon possible, where smoke plumes were contained within the PBL. Additionally, a significant portion of the lidar vertical cross-section is missing for the 0823a flight during the South Sugarloaf Fire, as depicted in **Fig. S4g**. In spite of the fire size indicating a megafire (Linley et al., 2022), the absence of the extinction coefficient data as well as in situ sampling in the downwind region (**Table 2**) leads to low estimates of SPH_{top} and SPH_{ext}.
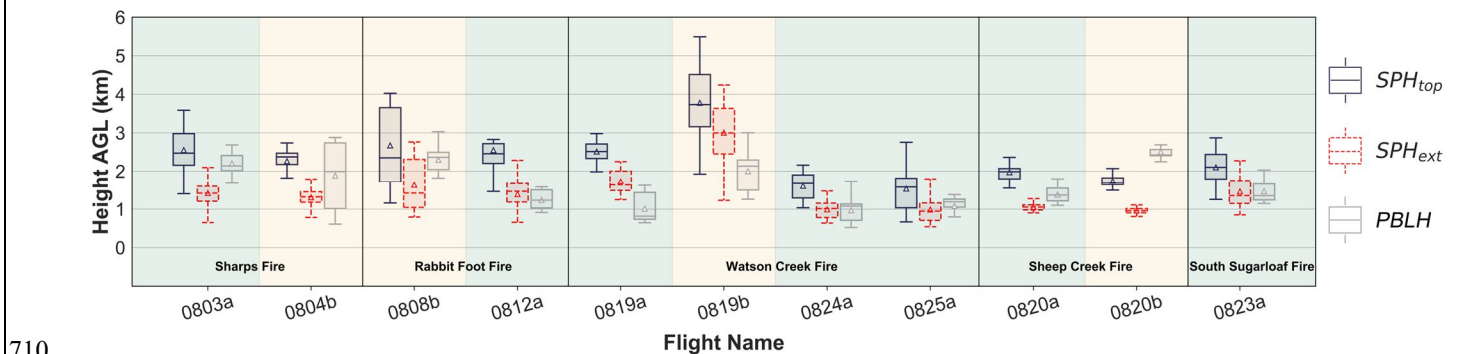
Figure 8: Box plots comparing the 30 min average modeled *PBLH* (grey) with the WCL-determined *SPH* using two different definitions (*SPH_top*, blue; *SPH_ext*, red) for the morning (shaded by green) and afternoon (shaded by yellow) flight missions. Each panel represents a single wildfire case. Upper and lower whiskers represent the 95th and 5th percentiles, respectively, while the box spans from the 25th percentile to the 75th percentile. The line inside the box represents the median (the 50th percentile), and the triangle indicates the mean of the range of height values. Note that the range of WCL *SPH* measurements for both morning (0820a) and afternoon (0820b) flight missions on August 20, 2018, is limited because only a small fraction of flight tracks is considered valid transects for reconstruction.

5 Summary and conclusions

The notion of *SPH* can be visualized as the vertical displacement from the ground to the upper atmosphere, marking the extent to which smoke plumes ascend. This parameter is vital for simulating the initial stage of plume production and predicting the potential spread of smoke from wildfires (e.g., Walter et al., 2016; Tang et al., 2022). ~~As~~ If smoke ~~crosses over~~ is emitted above the PBL, it tends to persist longer and ~~may~~ travel farther. Smoke emitted w~~W~~ithin the PBL~~H, the~~ adversely impacts ~~of smoke on~~ air quality ~~can be amplified~~ and increases ground-level air pollution concentrations.

Current efforts to study wildfire *SPH* mainly rely on the use of active lidar data and passive satellite sensor retrievals. However, these instruments face inherent spatial and temporal limitations, such as their inability to swiftly adapt to changes in fire and smoke plume behavior. Nonetheless, fusing multi-satellite products to ~~quantify~~ estimate *SPH* ~~and prove the existing aerosol layers~~ is still an evolving field. T~~Though t~~ransported smoke aerosols ~~may~~ can form complex, multilayer structures, but this study has shown that a single, uniform aerosol layer is encountered more frequently than previously assumed. This means that~~, making it possible~~ a single value can be used to describe the height of the aerosol layer ~~using a single numeric number~~. With this more straightforward representation, s~~S~~cientists can more readily incorporate aerosol layer data into climate and AQ models ~~with this more straightforward representation~~, including our earlier discussion of ~~and a concept of~~ an "effective *SPH*" ~~is further discussed~~ concept. We use~~d~~ two *SPH* definitions for comparisons~~,~~ since the *SPH* criterion varies between plume rise retrieval algorithms, given their diverse representations of aerosol vertical allocation that may not sufficiently reflect the real wildfire-associated smoke aerosol layering. W~~Then we~~ also employ~~ed~~ two different collocation methods to ~~deal with~~ provide ~~the~~ lidar-satellite collocated pairs. C~~The c~~ollocation uncertainties can be caused by the discrepancy between the coarse spatial resolution of the satellite retrieval algorithm and the fine-scale variability of wildfire smoke plume activity detected by high-resolution active lidar measurements.

Results in this paper reaffirm~~ed~~ that uncertainties in ~~various~~ multiple satellite-derived *SPH* products arise from different remote sensing techniques (Tosca et al., 2011; Flower and Kahn, 2017). The current state of satellite-based *SPH* ~~data~~ products is impacted by significant errors, which we ascribe mostly to either complex, multiple aerosol layers or thin, transparent plumes. The user recommendations and main conclusions drawn from this study are:

(1) The MAIAC PIH algorithm necessitates careful quality verification since its *SPH* retrievals are routinely lower than the lidar measurements, especially for MODIS/MAIAC-Aqua. We suggest selecting SPH_{ext}~~SPH^{ext}~~ as a suitable height metric to evaluate the MODIS/MAIAC-Terra product under conditions when the distance from the fire source is < 20 km and for AOD at 355 nm > 1.

(2) The MISR plume height climatology is promising to help locate wildfire-associated SPH_{top}~~SPH^{top}~~ and provide the best estimates over mountainous terrain. However, as WUS fires have become more frequent since the 2000s, the available MISR/MERLIN datasets are relatively minimal. Some challenges associated with using MISR/MERLIN include the limited timing of ~~The most striking problem is that the~~ MISR ~~observations~~ overpasses (which ~~can~~ only occur ~~be made~~ in the mid-late morning, local time), and ~~require~~ the labor-intensive nature of operating~~on of~~ the MINX software to digitize the smoke plumes.

(3) Both the VIIRS/ASHE and the TROPOMI/ALH products show great potential for characterizing SPH_{top}~~SPH^{top}~~ in a single homogenous aerosol-rich layer. An overestimation of *SPH* in the near-fire-event region and an underestimation of *SPH* in the downwind region still prevail ~~in AOD of different size bins~~. We find that large retrieval errors occur in the studied cases, underscoring the need for a robust quality screening approach related to the UVAI parameterization.

However, the performance evaluation of four satellite *SPH* ~~datasets~~ products presented here indicates only a weak to moderate correlation between passive satellite retrievals and airborne lidar observations. Deploying both passive and active sensors in tandem can offer a synergistic approach, filling gaps in our understanding of fire and smoke plume behavior by utilizing the unique strengths of each method. The lack of synchronization between satellite overpass times and variations in fire activity and aerosol layering is responsible for more than half of the collocated mismatches. It is expected that future satellites, equipped with active or passive sensors, can increase the chances of capturing a large wildfire event at its peak ~~increase~~, as exemplified by ~~(i.e., increased improved spatial and~~ temporal coverage of the Advanced Baseline Imager (ABI) on the geostationary satellites~~)~~. Notably, NASA's forthcoming aerosol investigations from space, such as ~~ACCP (Aerosol and Cloud, Convection and Precipitation)~~ AOS (Atmosphere Observing System), MAIA (Multi-Angle Imager for Aerosols), PACE (Plankton, Aerosol, Cloud, ocean Ecosystem), and TEMPO (Tropospheric Emissions: Monitoring of Pollution), are expected to play a pivotal role in this regard. By integrating data from multiple satellite systems as a potential solution to the synchronization issue, scientists can create a more comprehensive and improved picture of wildfire plume rise.

This study provides a preliminary comparison reference for multiple satellite-based *SPH* ~~data~~ applications. Our findings serve to connect smoke transport and AQ forecasting frameworks and future satellite missions that aim to quantify the vertical distribution of aerosols in the atmosphere, similar to the efforts of Raffuse et al. (2012), Solomos et al. (2015), Ke et al. (2021), and Kumar et al. (2022). We therefore encourage conversations between the communities involved in satellite remote sensing and atmospheric modeling to enhance the diversity of perspectives and foster a consensus on the measurement and comprehension of effective *SPH* with greater clarity.

Appendix A. Evaluation metrics for collocated lidar—satellite *SPH* comparison~~collocation~~

We evaluate the performance of a satellite *SPH* product against ~~with respect to~~ lidar observations using the following statistics: ~~the~~ mean bias (*MB*), ~~the~~ mean absolute error (*MAE*), ~~the~~ root mean square error (*RMSE*), coefficient of determination (R2) and ~~the~~ Pearson~~'s~~ correlation coefficient ~~score~~ (*r*). The metrics are calculated for *SPH* using ~~the~~ Eqs. (A1) to (~~A4~~A5):

$$MB = \overline{SPH_{lidar}} - \overline{SPH_{satellite}} - \overline{SPH_{lidar}}, \tag{A1}$$

$$MAE = \frac{\sum_{i=1}^{N}|SPH_{lidar,i} - SPH_{satellite,i}|}{N}, \tag{A2}$$

$$RMSE = \sqrt{\frac{\sum_{i=1}^{N}(SPH_{lidar,i} - SPH_{satellite,i})^2}{N}}, \tag{A3}$$

$$R^2 = 1 - \frac{\sum_{i=1}^{N}(SPH_{lidar,i} - SPH_{satellite,i})^2}{\sum_{i=1}^{N}(SPH_{lidar,i} - \overline{SPH_{lidar}})^2}, \tag{A4}$$

$$r = \frac{\sum_{i=1}^{N}(SPH_{lidar,i} - \overline{SPH_{lidar}})(SPH_{satellite,i} - \overline{SPH_{satellite}})}{\sqrt{\sum_{i=1}^{N}(SPH_{lidar,i} - \overline{SPH_{lidar}})^2}\sqrt{\sum_{i=1}^{N}(SPH_{satellite,i} - \overline{SPH_{satellite}})^2}}, \tag{A54}$$

, where $SPH_{lidar,i}$ is the ith collocated lidar measurement, $SPH_{satellite,i}$ is the ith collocated satellite ~~observation~~retrieval, $\overline{SPH_{lidar}}$ is the arithmetic mean of the collocated lidar measurements, $\overline{SPH_{satellite}}$ is the arithmetic mean of the collocated satellite ~~observations~~retrievals, *N* is the number of collocated pairs.

MB represents the average bias of a satellite *SPH* product but should be interpreted cautiously because positive and negative errors will cancel out. *MAE* measures the average over the sample absolute differences between lidar measurements and satellite ~~observations~~ retrievals where all individual differences have equal weight, without considering their direction. *RMSE* is the square root of the average of squared differences between lidar measurements and satellite ~~observations~~retrievals. *RMSE* ~~should be~~ is more useful when large outlier errors are particularly undesirable. Unlike *RMSE*, *MAE* is an unambiguous measure of average error magnitude. R^2 provides a statistical measure of how well a satellite *SPH* retrieval algorithm reflects the real-world conditions as measured by the more direct lidar technique. The closer R^2 is to 1, the more reliable the satellite retrieval is in representing the actual *SPH*. A negative R^2 happens when the performance of the satellite *SPH* product is worse than the mean absolute deviation of the lidar observations. *r* is a measure of the strength of a linear association between two variables, indicating that the ~~spatial~~ distribution of both lidar measurements and satellite ~~observations~~ retrievals for *SPH* has a similar ~~change~~ trend in the change. The best performance that a satellite *SPH* product would have for these evaluation metrics is: *MB* (km) = 0, *MAE* (km) = 0, *RMSE* (km) = 0, R^2 (unitless) = 1, and *r* (unitless) =1.

Appendix B. Additional statistical evaluation of four satellite-derived *SPH* products against WCL-determined *SPH* observations. Note that the satellite *SPH* information is only shown in one column to be compared with two distinctive WCL-determined *SPH* definitions. *STD* – standard deviation; *Q25* – lower quartile, 25% of the data lie below this value; *Q50* – median, 50% of the data lie below this value; *Q75* – upper quartile, 25% of the data lie above this value.

	WCL-Determined *SPH*	
	SPH$_{top}$	*SPH*$_{ext}$
MODIS-Terra/MAIAC		
# Collocated Pairs (spatial average)	163	
Lidar Observations Mean ± 1 *STD* (km)	2.162 ± 0.542	1.382 ± 0.368
Satellite Retrievals Mean ± 1 *STD* (km)	0.733 ± 0.447	
Lidar Observations ^{Max}/$_{Min}$ (km)	$^{3.903}$/$_{1.254}$	$^{2.253}$/$_{0.800}$
Satellite Retrievals ^{Max}/$_{Min}$ (km)	$^{2.114}$/$_{0.015}$	
Lidar Observations *Q25*, *Q50*, *Q75* (km)	1.776, 2.064, 2.508	1.131, 1.298, 1.581
Satellite Retrievals *Q25*, *Q50*, *Q75* (km)	0.438, 0.687, 0.903	
MODIS-Aqua/MAIAC		
# Collocated Pairs (spatial average)	114	
Lidar Observations Mean ± 1 *STD* (km)	2.686 ± 0.797	1.790 ± 0.644
Satellite Retrievals Mean ± 1 *STD* (km)	0.425 ± 0.262	
Lidar Observations ^{Max}/$_{Min}$ (km)	$^{4.215}$/$_{1.374}$	$^{3.422}$/$_{0.800}$
Satellite Retrievals ^{Max}/$_{Min}$ (km)	$^{0.935}$/$_{0.025}$	
Lidar Observations *Q25*, *Q50*, *Q75* (km)	2.063, 2.627, 3.350	1.274, 1.728, 2.325
Satellite Retrievals *Q25*, *Q50*, *Q75* (km)	0.192, 0.379, 0.697	
MISR/MERLIN		
# Collocated Pairs (spatial average)	90	
Lidar Observations Mean ± 1 *STD* (km)	2.216 ± 0.506	1.498 ± 0.449
Satellite Retrievals Mean ± 1 *STD* (km)	2.124 ± 0.625	
Lidar Observations ^{Max}/$_{Min}$ (km)	$^{2.982}$/$_{1.254}$	$^{2.253}$/$_{0.853}$
Satellite Retrievals ^{Max}/$_{Min}$ (km)	$^{3.029}$/$_{0.625}$	

Lidar Observations $Q25$, $Q50$, $Q75$ (km)	1.791, 2.204, 2.648	1.129, 1.428, 1.969
Satellite Retrievals $Q25$, $Q50$, $Q75$ (km)	1.658, 2.083, 2.801	
VIIRS/ASHE		
# Collocated Pairs (matched pair)	130	
Lidar Observations Mean ± 1 STD (km)	2.823 ± 0.999	1.895 ± 0.890
Satellite Retrievals Mean ± 1 STD (km)	2.707 ± 1.165	
Lidar Observations $^{Max}/_{Min}$ (km)	$^{5.493}/_{1.497}$	$^{4.003}/_{0.811}$
Satellite Retrievals $^{Max}/_{Min}$ (km)	$^{4.930}/_{0.231}$	
Lidar Observations $Q25$, $Q50$, $Q75$ (km)	1.977, 2.904, 3.318	1.094, 1.629, 2.489
Satellite Retrievals $Q25$, $Q50$, $Q75$ (km)	2.060, 2.683, 3.579	
TROPOMI/ALH		
# Collocated Pairs (matched pair)	127	
Lidar Observations Mean ± 1 STD (km)	2.677 ± 1.075	1.894 ± 0.936
Satellite Retrievals Mean ± 1 STD (km)	2.052 ± 0.588	
Lidar Observations $^{Max}/_{Min}$ (km)	$^{5.493}/_{1.374}$	$^{4.003}/_{0.734}$
Satellite Retrievals $^{Max}/_{Min}$ (km)	$^{3.425}/_{1.412}$	
Lidar Observations $Q25$, $Q50$, $Q75$ (km)	1.718, 2.337, 3.308	1.019, 1.542, 2.684
Satellite Retrievals $Q25$, $Q50$, $Q75$ (km)	1.546, 1.802, 2.431	

800   *Data availability.* The MODIS/MAIAC MCD19A2 Version 6.1 data product can be found at https:// earthdata.nasa.gov, last access: 10 May 2023. The Atmospheric Sciences Data Center hosts a web-based interface for freely downloading the MISR/MERLIN plume files at https://l0dup05.larc.nasa.gov/merlin/merlin#, last access: 10 August 2022. The TROPOMI/ALH Level 2 data are publicly available to users via Copernicus Open Access Hub at https://scihub.copernicus.eu/, last access: 9 February 2023. The VIIRS/ASHE data can be obtained from the VIIRS Deep Blue Aerosol Group (https://deepblue.gsfc.nasa.gov/,

805   last access: 28 July 2022). The BB-FLUX WCL data can be obtained from the official UWKA project website (http://www.atmos.uwyo.edu/uwka/projects/index.shtml, last access: 31 October 2022). Balloon sounding data are available from Atmospheric Soundings Wyoming Weather Website (https://weather.uwyo.edu/upperair/sounding.html, last access: 22 May 2023).

Author contribution. J.H.: Conceptualization; Investigation; Methodology; Lidar and satellite data curation; Software; Data
810   visualization and analysis; Writing - original draft; Writing - review & editing. S. M. L.: Investigation; Methodology; Writing - review & editing. M.D.: Methodology; Lidar data curation; Writing - review & editing. J. L.: Methodology; Satellite data curation; Writing - review & editing. H. A. H.: Conceptualization; Investigation; Methodology; Supervision; Funding acquisition; Writing - review & editing.

Competing interests. The authors declare that no known conflicts of interest, either financial or interpersonal, could have appeared
815   to influence the work reported in this paper.

Acknowledgements. This material is based on work supported, in part, by the National Science Foundation (NSF) Chemical, Bioengineering, Environmental, and Transport Systems (CBET) under grant number 2048423. We acknowledge high-performance

computing support from Cheyenne (doi:10.5065/D6RX99HX) provided by NCAR's Computational and Information Systems Laboratory, sponsored by ~~the National Science Foundation~~NSF. We thank the University of Wyoming King Air team for the successful deployment of the 2018 BB-FLUX project (PI: Rainer Volkamer). We acknowledge the use of imagery from the Worldview Snapshots application (https://wvs.earthdata.nasa.gov, last access: 15 June 2023), part of the Earth Observing System Data and Information System (EOSDIS). We appreciate the MODIS Adaptive Processing System (MODAPS) Team, the MISR Wildfire Smoke Plume Height Project, and the VIIRS Deep Blue Aerosol Group from NASA, and the TROPOMI Algorithm Team from the ESA for their efforts to create and maintain the satellite data records used in this paper.

References

Historic Perimeters Combined 2000-2018 GeoMAC: https://data-nifc.opendata.arcgis.com/datasets/nifc::historic-perimeters-combined-2000-2018-geomac/about, last access: 20 November 2023.

Ansmann, A., Baars, H., Chudnovsky, A., Mattis, I., Veselovskii, I., Haarig, M., Seifert, P., Engelmann, R., and Wandinger, U.: Extreme levels of Canadian wildfire smoke in the stratosphere over central Europe on 21–22 August 2017, Atmospheric Chem. Phys., 18, 11831–11845, 2018.

Ansmann, A., Ohneiser, K., Mamouri, R.-E., Knopf, D. A., Veselovskii, I., Baars, H., Engelmann, R., Foth, A., Jimenez, C., Seifert, P., and Barja, B.: Tropospheric and stratospheric wildfire smoke profiling with lidar: mass, surface area, CCN, and INP retrieval, Atmospheric Chem. Phys., 21, 9779–9807, https://doi.org/10.5194/acp-21-9779-2021, 2021.

Baars, H., Ansmann, A., Engelmann, R., and Althausen, D.: Continuous monitoring of the boundary-layer top with lidar, Atmospheric Chem. Phys., 8, 7281–7296, https://doi.org/10.5194/acp-8-7281-2008, 2008.

Baars, H., Radenz, M., Floutsi, A. A., Engelmann, R., Althausen, D., Heese, B., Ansmann, A., Flament, T., Dabas, A., and Trapon, D.: Californian wildfire smoke over Europe: A first example of the aerosol observing capabilities of Aeolus compared to ground-based lidar, Geophys. Res. Lett., 48, e2020GL092194, 2021.

Boone, J. T., Tosca, M., Galvin, A., Nastan, A., Schurman, D., Nair, P., Davidoff, S., Lombeyda, S., Mushkin, H., and Hendrie, M.: Redesigning for Research: Accessible Data Interaction with MISR Fire Plumes, AGU Fall Meeting Abstracts, GC51E-0840, 2018.

Brooks, I. M.: Finding boundary layer top: Application of a wavelet covariance transform to lidar backscatter profiles, J. Atmospheric Ocean. Technol., 20, 1092–1105, 2003.

Cao, C., De Luccia, F. J., Xiong, X., Wolfe, R., and Weng, F.: Early on-orbit performance of the visible infrared imaging radiometer suite onboard the Suomi National Polar-Orbiting Partnership (S-NPP) satellite, IEEE Trans. Geosci. Remote Sens., 52, 1142–1156, 2013a.

Cao, C., Xiong, J., Blonski, S., Liu, Q., Uprety, S., Shao, X., Bai, Y., and Weng, F.: Suomi NPP VIIRS sensor data record verification, validation, and long-term performance monitoring, J. Geophys. Res. Atmospheres, 118, 11–664, 2013b.

Cardil, A., Monedero, S., Ramírez, J., and Silva, C. A.: Assessing and reinitializing wildland fire simulations through satellite active fire data, J. Environ. Manage., 231, 996–1003, 2019.

Cheeseman, M., Ford, B., Volckens, J., Lyapustin, A., and Pierce, J.: The relationship between MAIAC smoke plume heights and surface PM, Geophys. Res. Lett., 47, e2020GL088949, 2020.

Chen, X., Wang, J., Xu, X., Zhou, M., Zhang, H., Garcia, L. C., Colarco, P. R., Janz, S. J., Yorks, J., and McGill, M.: First retrieval of absorbing aerosol height over dark target using TROPOMI oxygen B band: Algorithm development and application for surface particulate matter estimates, Remote Sens. Environ., 265, 112674, 2021.

Chimot, J., Veefkind, J. P., Vlemmix, T., De Haan, J. F., Amiridis, V., Proestakis, E., Marinou, E., and Levelt, P. F.: An exploratory study on the aerosol height retrieval from OMI measurements of the 477 nm O 2-O 2 spectral band using a neural network approach, Atmospheric Meas. Tech., 10, 783–809, 2017.

Chimot, J., Veefkind, J. P., Vlemmix, T., and Levelt, P. F.: Spatial distribution analysis of the OMI aerosol layer height: a pixel-by-pixel comparison to CALIOP observations, Atmospheric Meas. Tech., 11, 2257–2277, 2018.

Corradini, S. and Cervino, M.: Aerosol extinction coefficient profile retrieval in the oxygen A-band considering multiple scattering atmosphere. Test case: SCIAMACHY nadir simulated measurements, J. Quant. Spectrosc. Radiat. Transf., 97, 354–380, 2006.

Csiszar, I., Schroeder, W., Giglio, L., Ellicott, E., Vadrevu, K. P., Justice, C. O., and Wind, B.: Active fires from the Suomi NPP Visible Infrared Imaging Radiometer Suite: Product status and first evaluation results, J. Geophys. Res. Atmospheres, 119, 803–816, 2014.

Davis, K. J., Gamage, N., Hagelberg, C., Kiemle, C., Lenschow, D., and Sullivan, P.: An objective method for deriving atmospheric structure from airborne lidar observations, J. Atmospheric Ocean. Technol., 17, 1455–1468, 2000.

de Arruda Moreira, G., Guerrero-Rascado, J. L., Bravo-Aranda, J. A., Foyo-Moreno, I., Cazorla, A., Alados, I., Lyamani, H., Landulfo, E., and Alados-Arboledas, L.: Study of the planetary boundary layer height in an urban environment using a combination of microwave radiometer and ceilometer, Atmospheric Res., 240, 104932, 2020.

Deng, M., Wang, Z., Volkamer, R., Snider, J. R., Oolman, L., Plummer, D. M., Kille, N., Zarzana, K. J., Lee, C. F., and Campos, T.: Wildfire smoke observations in the western United States from the airborne Wyoming Cloud Lidar during the BB-FLUX project. Part I: Data description and methodology, J. Atmospheric Ocean. Technol., 39, 545–558, 2022a.

Deng, M., Volkamer, R. M., Wang, Z., Snider, J. R., Kille, N., and Romero-Alvarez, L. J.: Wildfire smoke observations in the western United States from the airborne Wyoming Cloud Lidar during the BB-FLUX project. Part II: Vertical structure and plume injection height, J. Atmospheric Ocean. Technol., 39, 559–572, 2022b.

Diner, D. J., Beckert, J. C., Reilly, T. H., Bruegge, C. J., Conel, J. E., Kahn, R. A., Martonchik, J. V., Ackerman, T. P., Davies, R., and Gerstl, S. A.: Multi-angle Imaging SpectroRadiometer (MISR) instrument description and experiment overview, IEEE Trans. Geosci. Remote Sens., 36, 1072–1087, 1998.

Ding, S., Wang, J., and Xu, X.: Polarimetric remote sensing in oxygen A and B bands: sensitivity study and information content analysis for vertical profile of aerosols, Atmospheric Meas. Tech., 9, 2077–2092, 2016.

Dubovik, O., Herman, M., Holdak, A., Lapyonok, T., Tanré, D., Deuzé, J., Ducos, F., Sinyuk, A., and Lopatin, A.: Statistically optimized inversion algorithm for enhanced retrieval of aerosol properties from spectral multi-angle polarimetric satellite observations, Atmospheric Meas. Tech., 4, 975–1018, 2011.

Dubuisson, P., Frouin, R., Dessailly, D., Duforêt, L., Léon, J.-F., Voss, K., and Antoine, D.: Estimating the altitude of aerosol plumes over the ocean from reflectance ratio measurements in the O2 A-band, Remote Sens. Environ., 113, 1899–1911, 2009.

Duforêt, L., Frouin, R., and Dubuisson, P.: Importance and estimation of aerosol vertical structure in satellite ocean-color remote sensing, Appl. Opt., 46, 1107–1119, 2007.

Flower, V. J. and Kahn, R. A.: Assessing the altitude and dispersion of volcanic plumes using MISR multi-angle imaging from space: Sixteen years of volcanic activity in the Kamchatka Peninsula, Russia, J. Volcanol. Geotherm. Res., 337, 1–15, 2017.

Fromm, M., Peterson, D., and Di Girolamo, L.: The primary convective pathway for observed wildfire emissions in the upper troposphere and lower stratosphere: A targeted reinterpretation, J. Geophys. Res. Atmospheres, 124, 13254–13272, 2019.

Gamage, N. and Hagelberg, C.: Detection and analysis of microfronts and associated coherent events using localized transforms, J. Atmospheric Sci., 50, 750–756, 1993.

Geddes, A. and Boesch, H.: Tropospheric aerosol profile information from high-resolution oxygen A-band measurements from space, Atmospheric Meas. Tech., 8, 859–874, 2015.

Goldberg, M. D., Kilcoyne, H., Cikanek, H., and Mehta, A.: Joint Polar Satellite System: The United States next generation civilian polar-orbiting environmental satellite system, J. Geophys. Res. Atmospheres, 118, 13–463, 2013.

Gonzalez-Alonso, L., Val Martin, M., and Kahn, R. A.: Biomass-burning smoke heights over the Amazon observed from space, Atmospheric Chem. Phys., 19, 1685–1702, 2019.

Gordon, H. R.: Atmospheric correction of ocean color imagery in the Earth Observing System era, J. Geophys. Res. Atmospheres, 102, 17081–17106, 1997.

Griffin, D., Sioris, C., Chen, J., Dickson, N., Kovachik, A., De Graaf, M., Nanda, S., Veefkind, P., Dammers, E., and McLinden, C. A.: The 2018 fire season in North America as seen by TROPOMI: aerosol layer height intercomparisons and evaluation of model-derived plume heights, Atmospheric Meas. Tech., 13, 1427–1445, 2020.

Hollstein, A. and Fischer, J.: Retrieving aerosol height from the oxygen A band: a fast forward operator and sensitivity study concerning spectral resolution, instrumental noise, and surface inhomogeneity, Atmospheric Meas. Tech., 7, 1429–1441, 2014.

Hsu, N. C., Herman, J., Bhartia, P., Seftor, C., Torres, O., Thompson, A., Gleason, J., Eck, T., and Holben, B.: Detection of biomass burning smoke from TOMS measurements, Geophys. Res. Lett., 23, 745–748, 1996.

Hsu, N. C., Herman, J., Torres, O., Holben, B., Tanre, D., Eck, T., Smirnov, A., Chatenet, B., and Lavenu, F.: Comparisons of the TOMS aerosol index with Sun-photometer aerosol optical thickness: Results and applications, J. Geophys. Res. Atmospheres, 104, 6269–6279, 1999.

Ichoku, C., Kahn, R., and Chin, M.: Satellite contributions to the quantitative characterization of biomass burning for climate modeling, Atmospheric Res., 111, 1–28, 2012.

Jeong, M. and Hsu, N. C.: Retrievals of aerosol single-scattering albedo and effective aerosol layer height for biomass-burning smoke: Synergy derived from "A-Train" sensors, Geophys. Res. Lett., 35, 2008.

Jeong, U., Tsay, S.-C., Hsu, N. C., Giles, D. M., Cooper, J. W., Lee, J., Swap, R. J., Holben, B. N., Butler, J. J., and Wang, S.-H.: Simultaneous retrievals of biomass burning aerosols and trace gases from the ultraviolet to near-infrared over northern Thailand during the 2019 pre-monsoon season, Atmospheric Chem. Phys., 22, 11957–11986, 2022.

Junghenn Noyes, K. T., Kahn, R. A., Sedlacek, A., Kleinman, L., Limbacher, J. A., and Li, Z.: Wildfire smoke particle properties and evolution, from space-based multi-angle imaging, Remote Sens., 12, 769, 2020.

Junghenn Noyes, K. T., Kahn, R. A., Limbacher, J. A., and Li, Z.: Canadian and Alaskan wildfire smoke particle properties, their evolution, and controlling factors, from satellite observations, Atmospheric Chem. Phys., 22, 10267–10290, 2022.

Kahn, R. A.: A Global Perspective on Wildfires, Eos, 101, https://doi.org/10.1029/2020EO138260, 2020.

Kahn, R. A., Li, W., Moroney, C., Diner, D. J., Martonchik, J. V., and Fishbein, E.: Aerosol source plume physical characteristics from space-based multiangle imaging, J. Geophys. Res. Atmospheres, 112, 2007.

Kahn, R. A., Chen, Y., Nelson, D. L., Leung, F., Li, Q., Diner, D. J., and Logan, J. A.: Wildfire smoke injection heights: Two perspectives from space, Geophys. Res. Lett., 35, 2008.

Ke, Z., Wang, Y., Zou, Y., Song, Y., and Liu, Y.: Global Wildfire Plume-Rise Data Set and Parameterizations for Climate Model Applications, J. Geophys. Res. Atmospheres, 126, e2020JD033085, 2021.

Koffi, B., Schulz, M., Bréon, F., Griesfeller, J., Winker, D., Balkanski, Y., Bauer, S., Berntsen, T., Chin, M., and Collins, W. D.: Application of the CALIOP layer product to evaluate the vertical distribution of aerosols estimated by global models: AeroCom phase I results, J. Geophys. Res. Atmospheres, 117, 2012.

Kumar, A., Pierce, R. B., Ahmadov, R., Pereira, G., Freitas, S., Grell, G., Schmidt, C., Lenzen, A., Schwarz, J. P., and Perring, A. E.: Simulating wildfire emissions and plume rise using geostationary satellite fire radiative power measurements: a case study of the 2019 Williams Flats fire, Atmospheric Chem. Phys., 22, 10195–10219, 2022.

Kylling, A., Vandenbussche, S., Capelle, V., Cuesta, J., Klüser, L., Lelli, L., Popp, T., Stebel, K., and Veefkind, P.: Comparison of dust-layer heights from active and passive satellite sensors, Atmospheric Meas. Tech., 11, 2911–2936, 2018.

Labonne, M., Bréon, F., and Chevallier, F.: Injection height of biomass burning aerosols as seen from a spaceborne lidar, Geophys. Res. Lett., 34, 2007.

Lee, J., Hsu, N. C., Bettenhausen, C., Sayer, A. M., Seftor, C. J., and Jeong, M. -J.: Retrieving the height of smoke and dust aerosols by synergistic use of VIIRS, OMPS, and CALIOP observations, J. Geophys. Res. Atmospheres, 120, 8372–8388, 2015.

Lee, J., Hsu, N. C., Bettenhausen, C., Sayer, A. M., Seftor, C. J., Jeong, M.-J., Tsay, S.-C., Welton, E. J., Wang, S.-H., and Chen, W.-N.: Evaluating the height of biomass burning smoke aerosols retrieved from synergistic use of multiple satellite sensors over Southeast Asia, Aerosol Air Qual. Res., 16, 2831, 2016.

Lee, J., Hsu, N. C., Sayer, A. M., Seftor, C. J., and Kim, W. V.: Aerosol layer height with enhanced spectral coverage achieved by synergy between VIIRS and OMPS-NM measurements, IEEE Geosci. Remote Sens. Lett., 18, 949–953, 2020.

Linley, G. D., Jolly, C. J., Doherty, T. S., Geary, W. L., Armenteras, D., Belcher, C. M., Bliege Bird, R., Duane, A., Fletcher, M., and Giorgis, M. A.: What do you mean,'megafire'?, Glob. Ecol. Biogeogr., 31, 1906–1922, 2022.

Liu, D., Chen, S., Cheng, C., Barker, H. W., Dong, C., Ke, J., Wang, S., and Zheng, Z.: Analysis of global three-dimensional aerosol structure with spectral radiance matching, Atmospheric Meas. Tech., 12, 6541–6556, 2019a.

Liu, M., Lin, J., Boersma, K. F., Pinardi, G., Wang, Y., Chimot, J., Wagner, T., Xie, P., Eskes, H., and Van Roozendael, M.: Improved aerosol correction for OMI tropospheric NO 2 retrieval over East Asia: constraint from CALIOP aerosol vertical profile, Atmospheric Meas. Tech., 12, 1–21, 2019b.

Liu, Y., Kochanski, A., Baker, K. R., Mell, W., Linn, R., Paugam, R., Mandel, J., Fournier, A., Jenkins, M. A., and Goodrick, S.: Fire behaviour and smoke modelling: model improvement and measurement needs for next-generation smoke research and forecasting systems, Int. J. Wildland Fire, 28, 570–588, 2019c.

Liu, Z., Winker, D., Omar, A., Vaughan, M., Kar, J., Trepte, C., Hu, Y., and Schuster, G.: Evaluation of CALIOP 532 nm aerosol optical depth over opaque water clouds, Atmospheric Chem. Phys., 15, 1265–1288, 2015.

Loría-Salazar, S. M., Sayer, A. M., Barnes, J., Huang, J., Flynn, C., Lareau, N., Lee, J., Lyapustin, A., Redemann, J., Welton, E. J., Wilkins, J. L., ... & Holmes, H. A.: Evaluation of Novel NASA Moderate Resolution Imaging Spectroradiometer and Visible Infrared Imaging Radiometer Suite Aerosol Products and Assessment of Smoke Height Boundary Layer Ratio During Extreme Smoke Events in the Western USA, J. Geophys. Res. Atmospheres, 126, e2020JD034180, https://doi.org/10.1029/2020JD034180, 2021.

Lu, Z., Wang, J., Xu, X., Chen, X., Kondragunta, S., Torres, O., Wilcox, E. M., and Zeng, J.: Hourly mapping of the layer height of thick smoke plumes over the western US in 2020 severe fire season, Front. Remote Sens., 2, 766628, 2021.

Lyapustin, A., Wang, Y., and Frey, R.: An automatic cloud mask algorithm based on time series of MODIS measurements, J. Geophys. Res. Atmospheres, 113, 2008.

Lyapustin, A., Wang, Y., Korkin, S., Kahn, R., and Winker, D.: MAIAC thermal technique for smoke injection height from MODIS, IEEE Geosci. Remote Sens. Lett., 17, 730–734, 2019.

Mamouri, R.-E. and Ansmann, A.: Potential of polarization lidar to provide profiles of CCN-and INP-relevant aerosol parameters, Atmospheric Chem. Phys., 16, 5905–5931, 2016.

Mardi, A. H., Dadashazar, H., MacDonald, A. B., Braun, R. A., Crosbie, E., Xian, P., Thorsen, T. J., Coggon, M. M., Fenn, M. A., and Ferrare, R. A.: Biomass burning plumes in the vicinity of the California coast: Airborne characterization of physicochemical properties, heating rates, and spatiotemporal features, J. Geophys. Res. Atmospheres, 123, 13–560, 2018.

McGill, M. J., Yorks, J. E., Scott, V. S., Kupchock, A. W., and Selmer, P. A.: The cloud-aerosol transport system (CATS): a technology demonstration on the international space station, Lidar remote sensing for environmental monitoring XV, 34–39, 2015.

Michailidis, K., Koukouli, M.-E., Siomos, N., Balis, D., Tuinder, O., Tilstra, L. G., Mona, L., Pappalardo, G., and Bortoli, D.: First validation of GOME-2/MetOp absorbing aerosol height using EARLINET lidar observations, Atmospheric Chem. Phys., 21, 3193–3213, 2021.

Michailidis, K., Koukouli, M.-E., Balis, D., Veefkind, J. P., De Graaf, M., Mona, L., Papagianopoulos, N., Pappalardo, G., Tsikoudi, I., and Amiridis, V.: Validation of the TROPOMI/S5P aerosol layer height using EARLINET lidars, Atmospheric Chem. Phys., 23, 1919–1940, 2023.

985 Moroney, C., Davies, R., and Muller, J.-P.: Operational retrieval of cloud-top heights using MISR data, IEEE Trans. Geosci. Remote Sens., 40, 1532–1540, 2002.

Muller, J.-P., Mandanayake, A., Moroney, C., Davies, R., Diner, D. J., and Paradise, S.: MISR stereoscopic image matchers: Techniques and results, IEEE Trans. Geosci. Remote Sens., 40, 1547–1559, 2002.

Nanda, S., Veefkind, J. P., De Graaf, M., Sneep, M., Stammes, P., De Haan, J. F., Sanders, A. F., Apituley, A., Tuinder, O., and
990 Levelt, P. F.: A weighted least squares approach to retrieve aerosol layer height over bright surfaces applied to GOME-2 measurements of the oxygen A band for forest fire cases over Europe, Atmospheric Meas. Tech., 11, 3263–3280, 2018a.

Nanda, S., De Graaf, M., Sneep, M., De Haan, J. F., Stammes, P., Sanders, A. F., Tuinder, O., Veefkind, J. P., and Levelt, P. F.: Error sources in the retrieval of aerosol information over bright surfaces from satellite measurements in the oxygen A band, Atmospheric Meas. Tech., 11, 161–175, 2018b.

995 Nanda, S., De Graaf, M., Veefkind, J. P., Ter Linden, M., Sneep, M., De Haan, J., and Levelt, P. F.: A neural network radiative transfer model approach applied to the Tropospheric Monitoring Instrument aerosol height algorithm, Atmospheric Meas. Tech., 12, 6619–6634, 2019.

Nanda, S., De Graaf, M., Veefkind, J. P., Sneep, M., ter Linden, M., Sun, J., and Levelt, P. F.: A first comparison of TROPOMI aerosol layer height (ALH) to CALIOP data, Atmospheric Meas. Tech., 13, 3043–3059, 2020.

1000 Nastan, A., Val, S., Tosca, M., Galvin, A., Ainsworth, H., and Diner, D. J.: Enabling New Research with MISR Wildfire Plume Height Project Data: The MISR Enhanced Research and Lookup INterface (MERLIN), AGU Fall Meeting Abstracts, A14F-01, 2022.

Nelson, D. L., Chen, Y., Kahn, R. A., Diner, D. J., and Mazzoni, D.: Example applications of the MISR INteractive eXplorer (MINX) software tool to wildfire smoke plume analyses, Remote sensing of fire: Science and application, 65–75, 2008.

1005 Nelson, D. L., Garay, M. J., Kahn, R. A., and Dunst, B. A.: Stereoscopic height and wind retrievals for aerosol plumes with the MISR INteractive eXplorer (MINX), Remote Sens., 5, 4593–4628, 2013.

Paugam, R., Wooster, M., Atherton, J., Freitas, S., Schultz, M., and Kaiser, J.: Development and optimization of a wildfire plume rise model based on remote sensing data inputs–Part 2, Atmospheric Chem. Phys. Discuss., 15, 9815–9895, 2015.

Paugam, R., Wooster, M., Freitas, S., and Val Martin, M.: A review of approaches to estimate wildfire plume injection height
1010 within large-scale atmospheric chemical transport models, Atmospheric Chem. Phys., 16, 907–925, 2016.

Raffuse, S. M., Craig, K. J., Larkin, N. K., Strand, T. T., Sullivan, D. C., Wheeler, N. J., and Solomon, R.: An evaluation of modeled plume injection height with satellite-derived observed plume height, Atmosphere, 3, 103–123, 2012.

Rosati, B., Herrmann, E., Bucci, S., Fierli, F., Cairo, F., Gysel, M., Tillmann, R., Größ, J., Gobbi, G. P., and Di Liberto, L.: Studying the vertical aerosol extinction coefficient by comparing in situ airborne data and elastic backscatter lidar, Atmospheric
1015 Chem. Phys., 16, 4539–4554, 2016.

Salomonson, V. V., Barnes, W., Xiong, J., Kempler, S., and Masuoka, E.: An overview of the Earth Observing System MODIS instrument and associated data systems performance, IEEE International Geoscience and Remote Sensing Symposium, 1174–1176, 2002.

Sanders, A. F., De Haan, J. F., Sneep, M., Apituley, A., Stammes, P., Vieitez, M., Tilstra, L., Koning, C., and Veefkind, J. P.:
1020 Evaluation of the operational Aerosol Layer Height retrieval algorithm for Sentinel-5 Precursor: application to O 2 A band observations from GOME-2A, Atmospheric Meas. Tech., 8, 4947–4977, 2015.

Sanders, A. F., De Haan, J. F., and Veefkind, J. P.: Retrieval of aerosol height from the oxygen A band with TROPOMI, Proc. Adv. Atmospheric Sci. Appl. Bruges Belg., 18–22, 2012.

Sanghavi, S., Martonchik, J., Landgraf, J., and Platt, U.: Retrieval of the optical depth and vertical distribution of particulate scatterers in the atmosphere using O_2 A-and B-band SCIAMACHY observations over Kanpur: a case study, Atmospheric Meas. Tech., 5, 1099–1119, 2012.

Schroeder, W., Oliva, P., Giglio, L., and Csiszar, I. A.: The New VIIRS 375 m active fire detection data product: Algorithm description and initial assessment, Remote Sens. Environ., 143, 85–96, 2014.

Sicard, M., Granados-Muñoz, M. J., Alados-Arboledas, L., Barragán, R., Bedoya-Velásquez, A. E., Benavent-Oltra, J. A., Bortoli, D., Comerón, A., Córdoba-Jabonero, C., and Costa, M. J.: Ground/space, passive/active remote sensing observations coupled with particle dispersion modelling to understand the inter-continental transport of wildfire smoke plumes, Remote Sens. Environ., 232, 111294, 2019.

Siomos, N., Balis, D. S., Poupkou, A., Liora, N., Dimopoulos, S., Melas, D., Giannakaki, E., Filioglou, M., Basart, S., and Chaikovsky, A.: Investigating the quality of modeled aerosol profiles based on combined lidar and sunphotometer data, Atmospheric Chem. Phys., 17, 7003–7023, https://doi.org/10.5194/acp-17-7003-2017, 2017.

Solomon, S., Dube, K., Stone, K., Yu, P., Kinnison, D., Toon, O. B., Strahan, S. E., Rosenlof, K. H., Portmann, R., and Davis, S.: On the stratospheric chemistry of midlatitude wildfire smoke, Proc. Natl. Acad. Sci., 119, e2117325119, 2022.

Solomos, S., Amiridis, V., Zanis, P., Gerasopoulos, E., Sofiou, F., Herekakis, T., Brioude, J., Stohl, A., Kahn, R., and Kontoes, C.: Smoke dispersion modeling over complex terrain using high resolution meteorological data and satellite observations–The FireHub platform, Atmos. Environ., 119, 348–361, 2015.

Sun, R., Krueger, S. K., Jenkins, M. A., Zulauf, M. A., and Charney, J. J.: The importance of fire–atmosphere coupling and boundary-layer turbulence to wildfire spread, Int. J. Wildland Fire, 18, 50–60, 2009.

Tang, W., Emmons, L. K., Buchholz, R. R., Wiedinmyer, C., Schwantes, R. H., He, C., Kumar, R., Pfister, G. G., Worden, H. M., and Hornbrook, R. S.: Effects of fire diurnal variation and plume rise on US Air quality during FIREX-AQ and WE-CAN Based on the multi-scale infrastructure for chemistry and aerosols (MUSICAv0), J. Geophys. Res. Atmospheres, 127, e2022JD036650, 2022.

Tedim, F., Leone, V., Amraoui, M., Bouillon, C., Coughlan, M. R., Delogu, G. M., Fernandes, P. M., Ferreira, C., McCaffrey, S., McGee, T. K., Parente, J., Paton, D., Pereira, M. G., Ribeiro, L. M., Viegas, D. X., and Xanthopoulos, G.: Defining Extreme Wildfire Events: Difficulties, Challenges, and Impacts, Fire, 1, https://doi.org/10.3390/fire1010009, 2018.

Torres, O., Bhartia, P., Herman, J., Ahmad, Z., and Gleason, J.: Derivation of aerosol properties from satellite measurements of backscattered ultraviolet radiation: Theoretical basis, J. Geophys. Res. Atmospheres, 103, 17099–17110, 1998.

Tosca, M., Randerson, J., Zender, C., Nelson, D., Diner, D., and Logan, J.: Dynamics of fire plumes and smoke clouds associated with peat and deforestation fires in Indonesia, J. Geophys. Res. Atmospheres, 116, 2011.

Toth, T. D., Zhang, J., Reid, J. S., and Vaughan, M. A.: A bulk-mass-modeling-based method for retrieving particulate matter pollution using CALIOP observations, Atmospheric Meas. Tech., 12, 1739–1754, 2019.

Val Martin, M., Kahn, R. A., and Tosca, M. G.: A global analysis of wildfire smoke injection heights derived from space-based multi-angle imaging, Remote Sens., 10, 1609, 2018.

Veefkind, J. P., Aben, I., McMullan, K., Förster, H., De Vries, J., Otter, G., Claas, J., Eskes, H., De Haan, J., and Kleipool, Q.: TROPOMI on the ESA Sentinel-5 Precursor: A GMES mission for global observations of the atmospheric composition for climate, air quality and ozone layer applications, Remote Sens. Environ., 120, 70–83, 2012.

Virtanen, T. H., Kolmonen, P., Sogacheva, L., Rodríguez, E., Saponaro, G., and de Leeuw, G.: Collocation mismatch uncertainties in satellite aerosol retrieval validation, Atmospheric Meas. Tech., 11, 925–938, 2018.

Walter, C., Freitas, S. R., Kottmeier, C., Kraut, I., Rieger, D., Vogel, H., and Vogel, B.: The importance of plume rise on the concentrations and atmospheric impacts of biomass burning aerosol, Atmospheric Chem. Phys., 16, 9201–9219, 2016.

1065 Wang, W. and Cao, C.: NOAA-20 VIIRS sensor data records geometric and radiometric calibration performance one year in-orbit, IGARSS 2019-2019 IEEE International Geoscience and Remote Sensing Symposium, 8485–8488, 2019.

Winker, D. M., Vaughan, M. A., Omar, A., Hu, Y., Powell, K. A., Liu, Z., Hunt, W. H., and Young, S. A.: Overview of the CALIPSO mission and CALIOP data processing algorithms, J. Atmospheric Ocean. Technol., 26, 2310–2323, 2009.

Wolfe, R. E., Lin, G., Nishihama, M., Tewari, K. P., Tilton, J. C., and Isaacman, A. R.: Suomi NPP VIIRS prelaunch and on-orbit

1070 geometric calibration and characterization, J. Geophys. Res. Atmospheres, 118, 11,508-11,521, https://doi.org/10.1002/jgrd.50873, 2013.

Wu, L., Hasekamp, O., van Diedenhoven, B., Cairns, B., Yorks, J. E., and Chowdhary, J.: Passive remote sensing of aerosol layer height using near-UV multiangle polarization measurements, Geophys. Res. Lett., 43, 8783–8790, 2016.

Xu, X., Wang, J., Wang, Y., Zeng, J., Torres, O., Yang, Y., Marshak, A., Reid, J., and Miller, S.: Passive remote sensing of altitude

1075 and optical depth of dust plumes using the oxygen A and B bands: First results from EPIC/DSCOVR at Lagrange-1 point, Geophys. Res. Lett., 44, 7544–7554, 2017.

Xu, X., Wang, J., Wang, Y., Zeng, J., Torres, O., Reid, J. S., Miller, S. D., Martins, J. V., and Remer, L. A.: Detecting layer height of smoke aerosols over vegetated land and water surfaces via oxygen absorption bands: hourly results from EPIC/DSCOVR in deep space, Atmospheric Meas. Tech., 12, 3269–3288, 2019.

1080